PHYSICAL REVIEW FLUIDS **7**, 053901 (2022)

Effect of surface temperature strips on the evolution of supersonic and hypersonic Mack modes: Asymptotic theory and numerical results

Lei Zhao
Department of Mechanics, Tianjin University, Tianjin, 300072, China

Ming Dong [*]
State Key Laboratory of Nonlinear Mechanics, Institute of Mechanics,
Chinese Academy of Sciences, Beijing 100190, China
and Sino-Russian Mathematics Center, Peking University, Beijing 100871, China

(Received 10 November 2021; accepted 21 April 2022; published 5 May 2022)

In this paper, we perform an asymptotic study of the effect of local surface temperature (heating or cooling) strips on oncoming inviscid Mack instability in supersonic or hypersonic boundary layers, which is presented for a canonic problem to shed light on the physical mechanisms by which surface imperfections impact on boundary-layer transition to turbulence. Assuming the Reynolds number to be sufficiently large, the change of the Mack amplitude due to interaction with the temperature strip is quantified by an explicit model developed by the multiscale analysis. It is revealed that the temperature strip plays an equivalent role as a roughness element by producing mean-flow distortions described by the triple-deck structure. However, the former renders a more complicated interaction with the Mack modes since the lower deck is compressible to leading-order accuracy. Based on this model, a systematic study for different control parameters is conducted. A heating strip enhances (or suppresses) the Mack modes with frequencies below (or above) a critical value, whereas a cooling strip plays the opposite role. The critical frequency is found to be the most unstable frequency of the second mode, instead of the synchronization frequency as was found in some previous works for both roughness and temperature-strip configurations. A few phenomena in contrast to the roughness configuration are observed and readily explained by the asymptotic model. The asymptotic predictions agree favorably with the Harmonic linearized Navier-Stokes calculations and the direct numerical simulations, especially when the wall temperature is low.

DOI: 10.1103/PhysRevFluids.7.053901

I. INTRODUCTION

Since the laminar skin friction and heat transfer are remarkably smaller than those of the turbulent flow, the laminar state would obviously be more desirable than turbulence. Under high-altitude flying conditions for which the environmental perturbations are rather weak, transition usually follows a natural route, in which four stages, namely, receptivity (excitation of normal instability modes by external perturbations), linear instability (exponential amplification of normal modes), nonlinear breakdown (nonlinear interactions of perturbations, rapid distortion of the mean flow, and breakdown of the laminar flow), and turbulence, appear in sequence [1]. The normal instability modes could be the Tollmien-Schlichting (T-S) wave in subsonic boundary layers, or the Mack first and second modes in supersonic and hypersonic boundary layers [2]. To delay transition to

---

[*] dongming@imech.ac.cn

turbulence, one needs to minimize the level of the initial amplitudes of the normal modes in the receptivity stage or reduce the normal-mode growth rates in the linear instability stage. Therefore, laminar-flow control (LFC) based on the above concepts has been an attractive topic in the field of aeronautics and aerospace for decades [3].

Usually, LFC is implemented by introducing localized surface imperfections on the flying vehicles, which may promote or delay transition due to two physical mechanisms [4,5]. The first one is the local receptivity, which is referred to as the excitation of the boundary-layer instability modes due to interaction with the freestream perturbations. For incompressible and subsonic flows, the local receptivity of the T-S modes can be formulated by the triple-deck formalism; see for instance the roughness-sound interaction [6,7] and the roughness-vorticity interaction [8–10]. Such a framework was extended to the transonic configuration [11], and even to the supersonic configuration for the excitation of the first Mack modes with large oblique angles $\Theta \equiv \tan^{-1}(\beta/\alpha_r)$ [12], where β and α_r denote the spanwise and streamwise wave numbers, respectively. Interestingly, it was found from the latter work that if the incident angle of the freestream sound wave is around a particular value, the receptivity efficiency could be much stronger. However, the receptivity mechanism of the first Mack modes with small oblique angles and the second Mack modes is quite different due to their inviscid nature, and Ref. [13] was the first to develop an asymptotic theory to reveal the local receptivity mechanism of the supersonic inviscid modes due to roughness-sound interaction.

The second mechanism is the local scattering of the instability modes, in which the local surface imperfection interacts with the oncoming instability, leading to an abrupt change of its amplitude in a localized region. In subsonic boundary layers, the scattering of the T-S modes by two-dimensional (2D) localized roughness was formulated based on the triple-deck formalism by Wu and Dong [14]. It was found that the T-S modes are always enhanced by both humps and indentations, leading to premature transition eventually, which agrees with the numerical observations [15]. However, for hypersonic boundary layers, an experimental study [16] reported that the transition could be either promoted or delayed by 2D roughness depending on its location. Subsequent direct numerical simulations (DNSs) [17,18] showed that roughness could enhance the oncoming second mode when its frequency is lower than the synchronization frequency (at which the phase speeds of the fast and slow modes, originated from the fast and slow acoustic wave, respectively, intersect), while the stabilizing effect appears for a supercritical frequency. Using the harmonic linearized Navier-Stokes (HLNS) approach, Zhao, Dong, and Yang [19] presented a systematic study of the scattering of Mack modes by localized humps and indentations, confirming the aforementioned DNS results. Moreover, some interesting phenomena were reported, e.g., an indentation plays the same stabilizing or destabilizing role as a hump, but its scattering effect is quantitatively weaker; increase of the roughness width does not lead to an appreciable change of the scattering effect. These phenomena were explained by an asymptotic theory presented by Dong and Zhao [20], and the theoretical predictions were confirmed to be in good agreement with the HLNS calculations.

Among the many control strategies, surface suction may be the most extensively studied one in literature [21]. Reynolds and Saric [22] conducted an early experiment on the development of T-S waves in a low-speed boundary layer with porous suction panels, which confirmed the stabilizing effect of suction. The experimental data agrees favorably with the theoretical predictions [23]. It was found that the steady suction induces a certain mean-flow distortion near the suction panels, which can be predicted by the triple-deck theory; linear stability analysis of the distorted mean flow shows smaller growth rates of the unstable T-S waves, leading to delay of transition to turbulence. However, as the mass flux increases, the accuracy of the theoretical predictions become poorer, and a more proper approach which takes into account the “local scattering effect” of the abrupt suction panel was developed by Ref. [24]. Applications of suction on different circumstances, including three-dimensional (3D) and compressible configurations and the combined effects with other surface imperfections, are investigated subsequently [25–31]. Recently, Schrauf and von Geyr [3] reported a Mach-0.78 flight test with a simplified hybrid LFC system on an A320 aircraft performed in April–May 2018. Transition was found to be delayed when moderate suction was

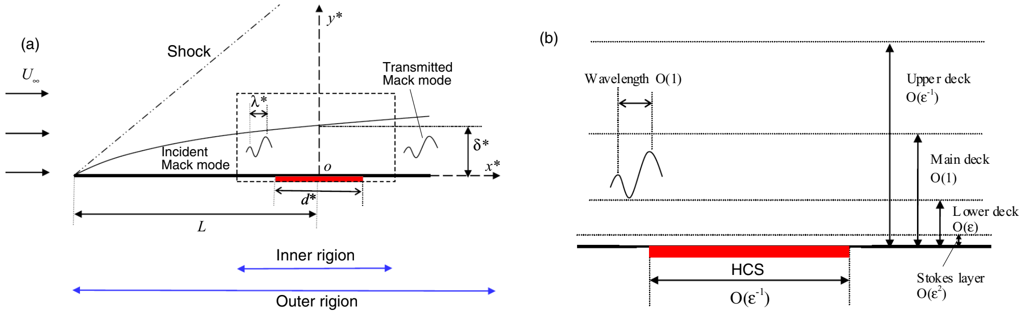

FIG. 1. Physical model to be studied and the characteristic length scales, where the red region at the wall denotes the heating/cooling strip. Panel (b) shows the multiscale structure of the rectangular zone of panel (a).

introduced, and the evolution of the T-S waves was compared favorably to predictions by the linear stability theory (LST).

As another representative surface imperfection, heating or cooling strips frequently appear at the wall of compressible boundary layers. Early asymptotic solutions of the linear instability [32] identified that surface cooling could suppress the growth of the boundary-layer perturbations, which was confirmed in subsonic boundary layers [33]. For supersonic or hypersonic boundary layers, Mack [34], through careful numerical calculations, reported that only the first mode is suppressed by wall cooling, but the second mode and higher-order modes are enhanced. However, for a localized temperature strip, the situation could be more complicated. Through experimental and numerical investigations of a Mach 6 boundary layer on a cone, for which the second mode plays the dominant role in the transition process, a few subsequent works [35–37] found that a localized heating (cooling) panel accelerates (delays) transition, in contrast to the observations for uniform heating (cooling) cases [34]. They also remarked that the location of the strip may also be a crucial factor. Through DNSs, Zhao *et al.* [38] studied the impact of narrow heating or cooling strips on oncoming Mack modes in a Mach 6 boundary layer. Interestingly, when a heating (cooling) strip is located upstream of the synchronization point of the dominant perturbation, the transition would be promoted (delayed), while the opposite is true when it is located downstream of the synchronization point. Such effects are somewhat similar to the roughness configuration mentioned earlier. However, there is also a notable discrepancy, namely, a hump and an indentation play the same stabilizing or destabilizing role on the oncoming Mack modes with the same frequency band, although the effect for a hump is stronger, however, a heating strip plays an opposite role to a cooling strip. It seems to be puzzling unless an in-depth theoretical analysis is performed, which is the main task of the present work.

The asymptotic analysis to be presented in this paper is an extension of the asymptotic theory developed in Ref. [20], in which the scattering effect was quantified by an explicit model based on the multiscale analysis. However, being different from the roughness configuration [20], the lower deck distorted by the temperature strip is compressible to leading-order accuracy, rendering a more complicated interaction with the oncoming Mack modes.

II. MATHEMATICAL DESCRIPTION

A. Physical problem

We consider a supersonic or hypersonic boundary layer over a semi-infinite flat plate with zero angle of attack, as sketched in Fig. 1(a). The oncoming stream is assumed to be a perfect gas, whose velocity and kinematic viscosity are U_∞ and ν_∞, respectively. In what follows, the subscript ∞ denotes the oncoming quantities. The plate is assumed to be isothermal, except at the surface heating or cooling strip (HCS). The distance from the plate leading edge to the HCS center is L, and the width of the HCS is d^*. In this paper, the asterisk is referred to as the dimensional quantities. The HCS intensity is quantified by Θ_m^*. We assume the incident Mack mode to be inviscid, with a frequency ω^* and a wavelength λ^*, and the perturbation, after interacting with the HCS, is referred to as the transmitted Mack mode.

The displacement thickness of the boundary layer at the HCS center, $\delta^* = \Delta\sqrt{\nu_\infty L/U_\infty}$, is taken to be the characteristic length for normalization, where Δ is a constant obtained from the compressible Blasius similarity solution. Δ increases with the oncoming Mach number and the wall temperature, as will be shown in Table I. Practically, Δ is much greater than 1 in hypersonic configurations. For instance, $\Delta \approx 16.9$ (10.4) for a Mach 5.92 (4.5) boundary layer with an adiabatic wall. The problem is described in the Cartesian coordinate system (x^*, y^*, z^*), with its origin located at the HCS center; the coordinates are normalized as $(x, y, z) = (x^*, y^*, z^*)/\delta^*$. The velocity field $\boldsymbol{u}^* = (u^*, v^*, w^*)$, density ρ^* and temperature T^* are normalized by U_∞, ρ_∞ and T_∞, respectively, and the pressure p^* and time t^* are normalized by $\rho_\infty U_\infty^2$ and δ^*/U_∞, respectively. The Reynolds and Mach numbers are defined as $R = U_\infty\delta^*/\nu_\infty = \Delta\sqrt{U_\infty L/\nu_\infty}$ and $M = U_\infty/a_\infty$, respectively, where a_∞ denotes the sound speed of the oncoming stream. In this paper, we take $R \gg 1$ and $M > 1$. For convenience, we introduce a small parameter

$$\epsilon = R^{-1/4} \ll 1. \tag{1}$$

For simplicity, we assume the HCS to be 2D, but the oncoming Mack modes could be either 2D or three-dimensional (3D).

B. Governing equations

For a perfect gas with a constant ratio of specific heat γ, the dimensionless Navier-Stokes (N-S) equations are [31]

$$\begin{aligned}
&\frac{\partial\rho}{\partial t} + \nabla\cdot(\rho\boldsymbol{u}) = 0,\\
&\rho\frac{\partial\boldsymbol{u}}{\partial t} + \rho(\boldsymbol{u}\cdot\nabla)\boldsymbol{u} = -\nabla p + \frac{1}{R}\nabla\cdot(2\mu\mathbf{e}) + \frac{1}{R}\nabla\left[\left(\mu_0 - \frac{2}{3}\mu\right)\nabla\cdot\boldsymbol{u}\right],\\
&\rho\frac{\partial T}{\partial t} + \rho(\boldsymbol{u}\cdot\nabla)T = (\gamma-1)M^2\left[\frac{\partial p}{\partial t} + (\boldsymbol{u}\cdot\nabla)p\right] + \frac{\nabla\cdot(\mu\nabla T)}{\mathrm{Pr}R} + \frac{(\gamma-1)M^2\Phi}{R},\\
&\gamma M^2 p = \rho T,
\end{aligned} \tag{2}$$

where the strain rate tensor $\mathbf{e}$ and the dissipation function Φ are expressed as $\mathrm{e}_{ij} = \frac{1}{2}(\frac{\partial u_i}{\partial x_j} + \frac{\partial u_j}{\partial x_i})$, $\Phi = 2\mu\mathbf{e}:\mathbf{e} + (\mu_0 - \frac{2}{3}\mu)(\nabla\cdot\boldsymbol{u})^2$, Pr is the Prandtl number, $\mu = \mu(T)$ the dimensionless dynamic viscous coefficient, and $\mu_0 = \mu_0^*/\mu_\infty$ the dimensionless second viscosity. The Sutherland's viscosity law is selected,

$$\mu(T) = \frac{(1+\bar{C})T^{3/2}}{T+\bar{C}}, \tag{3}$$

with $\bar{C} = 110.4\mathrm{K}/T_\infty$. We take $\gamma = 1.4$, $\mathrm{Pr} = 0.72$, and $\mu_0 = 0$.

The instantaneous flow field is expressed as a superposition of the mean flow $\bar{\boldsymbol{\varphi}}$ and an unsteady perturbation $\tilde{\boldsymbol{\varphi}}$,

$$\boldsymbol{\varphi}(x, y, z, t) = \bar{\boldsymbol{\varphi}}(x, y) + \tilde{\boldsymbol{\varphi}}(x, y, z, t), \tag{4}$$

where $\boldsymbol{\varphi} = (u, v, w, \rho, T, p)$. For an isothermal surface without any HCS, the steady mean flow can be described by the compressible Blasius similarity solution, $(\bar{U}_B, \Delta^2\epsilon^4\bar{V}_B)(\bar{x}, y)$, as shown in the Appendix of Ref. [39].

TABLE I. Key parameters characterizing the base flow.

Case	Mach number M	Oncoming temperature T_∞	Wall temperature T_w	Temperature ratio $\frac{T_w}{T_{ad}}$	Shape constant Δ	Nominal thickness δ_{99}	Location of GIP y_c	Velocity at GIP U_c	Wall shear $U_B'(0)$	Wall temperature gradiant $T_B'(0)$	Description
M1T1	4.5	65.15K	4.4	1.0	10.4	1.30	1.07	0.89	0.830	0	adiabatic
M1T2	4.5	65.15K	3.3	0.75	8.45	1.37	1.05	0.86	0.867	0.872	cold wall
M1T3	4.5	65.15K	2.2	0.5	6.44	1.49	1.00	0.80	0.957	1.90	cold wall
M1T4	4.5	65.15K	1.1	0.25	4.31	1.74	–	–	1.31	3.88	very cold wall
M1T5	4.5	226.5K	4.4	1.0	8.70	1.32	1.02	0.87	0.87	0	adiabatic
M1T6	4.5	226.5K	3.3	0.75	7.26	1.40	0.99	0.83	0.89	0.89	cold wall
M1T7	4.5	226.5K	2.2	0.5	5.72	1.52	0.89	0.73	0.95	1.88	cold wall
M1T8	4.5	226.5K	1.1	0.25	4.03	1.76	–	–	1.17	3.46	very cold wall
M2T1	5.92	48.69K	6.95	1.0	16.9	1.18	1.08	0.94	0.86	0	adiabatic
M2T2	5.92	48.69K	5.21	0.75	14.0	1.22	1.07	0.92	0.90	1.39	cold wall
M2T3	5.92	48.69K	3.48	0.5	10.8	1.29	1.07	0.90	1.0	3.1	cold wall
M2T4	5.92	48.69K	1.74	0.25	7.47	1.43	1.05	0.85	1.38	6.39	very cold wall
M2T9	5.92	226.5K	0.5	0.072	4.50	1.66	–	–	2.6	15.0	Extremely cold wall

III. ASYMPTOTIC DESCRIPTION FOR THE MACK-HCS INTERACTION

As shown in Fig. 1(a), there are two asymptotic regions in the streamwise direction, an inner region where $x = O(\epsilon^{-1})$, and an outer region where $x^* = O(L)$ [or $x = O(\epsilon^{-4}\Delta^{-2})$]. The two regions match asymptotically as shown in Appendix A of Ref. [20]. In this paper, we will only demonstrate the interaction in the inner region, whose asymptotic structure is depicted in Fig. 1(b). For convenience, we introduce a local coordinate,

$$X = \epsilon x = O(1). \tag{5}$$

A. HCS-induced mean-flow distortion: Triple-deck structure

In the asymptotic analysis, we assume the intensity of the HCS $\Theta_m^* = O(T_w^*)$, and therefore, introduce an $O(1)$ parameter to characterize the dimensionless HCS amplitude,

$$\Theta_m = \Theta_m^*/T_w^*. \tag{6}$$

Θ_m is positive for a heating strip or negative for a cooling strip. For demonstration, we assume a uniform distribution of HCS, and so the temperature at the wall is expressed as

$$\bar{T}(X,0) = \begin{cases} T_w(1+\Theta_m) & \text{for } |X| \leqslant d/2, \\ T_w & \text{otherwise,} \end{cases} \tag{7}$$

where $T_w \equiv T_w^*/T_\infty$ is the dimensionless wall temperature away from the HCS, and $d = \epsilon d^*/\delta^*$ characterizes the width of the HCS. To keep the temperature to be positive throughout the flow field, we take $\Theta_m > -1$. Of course our theory is also applicable for other types of temperature distribution.

The mean flow distorted by an HCS exhibits a triple-deck structure, the lower deck where $y = O(\epsilon)$, a main deck where $y = O(1)$ and an upper deck where $y = O(\epsilon^{-1})$, which is the same as that by roughness as in Ref. [20]. However, the properties of the lower-deck governing equations are different. For the latter configuration, the surface roughness induces a velocity distortion [of $O(\epsilon)$] in the lower deck, producing directly an $O(\epsilon)$ slip velocity to the main-deck solution through the displacement effect, and the variations of the density and temperature are passive and small, rendering an incompressible nature of the lower deck; see Refs. [20,40]. However, for the former configuration, the HCS induces a temperature distortion in the lower deck, which is of the same order as the temperature at the wall, $\Theta_m = O(1)$. Therefore, the energy equation in the lower deck comes to the leading order, implying that the lower deck becomes fully compressible. Fortunately, the $O(1)$ temperature distortion is restricted within the lower deck, which damps in the outer limit and do not produce a temperature distortion to the main deck directly, as will be shown in Sec. III A 2. Simultaneously, the $O(1)$ temperature distortion drives an $O(\epsilon)$ velocity distortion in the lower deck, which, being the same as that for the roughness configuration, induces an $O(\epsilon)$ distortion in the main deck through the displacement effect. From this point of view, we conclude that the HCS behaves like an equivalent roughness by producing an $O(\epsilon)$ mean-flow distortion to the main-deck mean flow, but to calculate the displacement function is more complicated due to the coupling of the momentum and energy equations in the lower deck.

The solutions of the compressible triple-deck equations have already been reported by a few previous works. Lipatov [41] first presented the mathematical details to demonstrate the effect of localized, unsteady heating elements on the flow properties. Assuming the heating intensity to be small, Koroteev and Lipatov [42] solved the linearized compressible triple-deck equations analytically; later numerical solutions [43–45] were able to deal with nonlinearities of the compressible triple-deck system. Using this system, the cancellation of the T-S waves by localized heating elements in subsonic boundary layers was studied by Brennan, Gajjar, and Hewitt [46]. The present work will follow these numerical approaches to obtain the mean-flow distortion induced by the HCSs. However, to be more accurate to compare with the finite-R calculations, we employ the Sutherland's viscosity law Eq. (3) and a realistic Prandtl number, instead of the Chapman viscosity law and unity Prandtl number employed by the previous works. It needs to be noted that such a change does not lead to any new regime, and the only advantage is to provide a more accurate asymptotic prediction in quantity.

1. Main deck

In the main layer where $y = O(1)$, the velocity field, density, temperature, and pressure of the mean flow are expressed as

$$\bar{\varphi} = \left(U_B, 0, 0, \frac{1}{T_B}, T_B, \frac{1}{\gamma M^2}\right) + \epsilon(U_1, \epsilon V_1, 0, R_1, T_1, 0) + \cdots , \tag{8}$$

where $U_B(y) = \bar{U}_B(0, y)$ and $T_B(y) = \bar{T}_B(0, y)$ represent the streamwise velocity and temperature of the Blasius solution at $x = 0$, respectively. Note that in Ref. [20], the expansion also includes the $O(\epsilon^3\Delta^2)$ terms, which were introduced for matching with the outer layer. The mean-flow distortions are given by [40,47,48]

$$U_1 = A(X)U_B', \quad V_1 = -A'(X)U_B, \quad R_1 = -A(X)T_B'/T_B^2, \quad T_1 = A(X)T_B', \tag{9}$$

where the prime throughout this paper denotes the derivative with respect to its argument, and A is the displacement function to be determined. To match with the boundary conditions at the wall, we need to consider a thinner lower deck.

2. Lower deck

In the lower deck, where $Y = \epsilon^{-1}y = O(1)$, we renormalize the coordinates as

$$\tilde{X} = \mathcal{R}_X X, \quad \tilde{Y} = \mathcal{R}_Y Y, \tag{10}$$

where

$$\mathcal{R}_X = \lambda^{5/4}(M^2 - 1)^{3/8}\bar{C}^{-3/8}T_w^{-3/2} = O(1), \quad \mathcal{R}_Y = \lambda^{3/4}(M^2 - 1)^{1/8}\bar{C}^{-5/8}T_w^{-3/2} = O(1), \tag{11}$$

with $\lambda \equiv \bar{C}^{1/2}T_w U_{B,y}(0)$ being the wall shear of the Blasius profile, $\bar{C} = \mu_w/T_w$ and $\mu_w = \mu(T_w)$. The width of the surface HCS is rescaled as

$$D = \mathcal{R}_X d. \tag{12}$$

According to Eq. (10), the temperature distribution at the wall Eq. (7) is recast to

$$\bar{T}(\tilde{X}, 0) = T_w[1 + \Theta_m f(\tilde{X})], \quad f(\tilde{X}) = \begin{cases} 1 & \text{for } |\tilde{X}| \leqslant D/2, \\ 0 & \text{otherwise.} \end{cases} \tag{13}$$

The velocity field, pressure, temperature, density, and viscosity are rescaled as

$$(\bar{U}, \bar{V}, \bar{P}, \bar{T}, \bar{R}, \bar{\mu}) = \left(\epsilon\mathcal{R}_U^{-1}\tilde{U}, \epsilon^3\mathcal{R}_V^{-1}\tilde{V}, \frac{1}{\gamma M^2} + \epsilon^2\mathcal{R}_P^{-1}\tilde{P}, T_w\tilde{T}, \frac{1}{T_w}\tilde{R}, \mu_w\tilde{\mu}\right) + \cdots , \tag{14}$$

where

$$\begin{aligned} \mathcal{R}_U &= \lambda^{-1/4}(M^2 - 1)^{1/8}\bar{C}^{-1/8}T_w^{-1/2}, \\ \mathcal{R}_V &= \lambda^{-3/4}(M^2 - 1)^{-1/8}\bar{C}^{-3/8}T_w^{-1/2}, \\ \mathcal{R}_P &= \lambda^{-1/2}(M^2 - 1)^{1/4}\bar{C}^{-1/4}. \end{aligned} \tag{15}$$

From the Sutherland's viscosity law Eq. (3), we obtain

$$\tilde{\mu} = \frac{(T_w + \bar{C})\tilde{T}^{3/2}}{T_w\tilde{T} + \bar{C}}. \tag{16}$$

Substituting the rescaled coordinates and flow field into the N-S equations and retaining the leading-order terms, we obtain the boundary-layer equations,

$$(\tilde{R}\tilde{U})_{\tilde{X}} + (\tilde{R}\tilde{V})_{\tilde{Y}} = 0, \quad \tilde{R}(\tilde{U}\tilde{U}_{\tilde{X}} + \tilde{V}\tilde{U}_{\tilde{Y}}) + \tilde{P}_{\tilde{X}} - (\tilde{\mu}\tilde{U}_{\tilde{Y}})_{\tilde{Y}} = 0, \tag{17a,b}$$

$$\tilde{P}_{\tilde{Y}} = 0, \quad \tilde{R}(\tilde{U}\tilde{T}_{\tilde{X}} + \tilde{V}\tilde{T}_{\tilde{Y}}) - \frac{1}{\mathrm{Pr}}(\tilde{\mu}\tilde{T}_{\tilde{Y}})_{\tilde{Y}} = 0, \quad \tilde{R}\tilde{T} = 1. \tag{17c,d,e}$$

In contrast to the roughness configuration, system Eq. (17) is compressible. The variations of the density and temperature influence the continuity and momentum equations, whereas the velocity field influences the convection terms of the energy equation, rendering a coupled nature of the velocity and temperature. The upstream boundary conditions read

$$(\tilde{U}, \tilde{V}, \tilde{T}, \tilde{R}, \tilde{P}) \to (\tilde{Y}, 0, 1, 1, 0) \quad \text{as } \tilde{X} \to -\infty, \tag{18}$$

whereas the boundary conditions at the wall read

$$\tilde{U}(\tilde{X}, 0) = \tilde{V}(\tilde{X}, 0) = 0, \quad \tilde{T}(\tilde{X}, 0) = 1 + \Theta_m f(\tilde{X}). \tag{19a,b,c}$$

Matching with the main-deck solution, we obtain

$$\tilde{U} \to \tilde{Y} + \tilde{A}, \quad \tilde{T} \to 1 \quad \text{as } \tilde{Y} \to \infty, \tag{20a,b}$$

where $\tilde{A}$ is the rescaled displacement function. $\tilde{A}$ is related to A (defined in Sec. III A) via

$$\tilde{A} = \mathcal{R}_Y A. \tag{21}$$

The nonlinear system Eq. (17) can be solved by numerical approaches. To ease the numerical procedure, we introduce the Dorodnitzyn-Howarth transformation,

$$\tilde{Y}_{\mathrm{DH}} = \int_0^{\tilde{Y}} \tilde{R} d\tilde{Y}, \quad \tilde{V}_{\mathrm{DH}} = \tilde{R}\tilde{V} + \frac{\partial \tilde{Y}_{\mathrm{DH}}}{\partial \tilde{X}} \tilde{U}. \tag{22}$$

Then, the system Eq. (17) is reduced to

$$\tilde{U}_{\tilde{X}} + \tilde{V}_{\mathrm{DH}, \tilde{Y}_{\mathrm{DH}}} = 0, \quad \tilde{U}\tilde{U}_{\tilde{X}} + \tilde{V}_{\mathrm{DH}}\tilde{U}_{\tilde{Y}_{\mathrm{DH}}} + \tilde{T}\tilde{P}_{\tilde{X}} - (\tilde{\mu}_{\mathrm{DH}}\tilde{U}_{\tilde{Y}_{\mathrm{DH}}})_{\tilde{Y}_{\mathrm{DH}}} = 0, \tag{23a,b}$$

$$\tilde{P}_{\tilde{Y}_{\mathrm{DH}}} = 0, \quad \tilde{U}\tilde{T}_{\tilde{X}} + \tilde{V}_{\mathrm{DH}}\tilde{T}_{\tilde{Y}_{\mathrm{DH}}} - \frac{1}{\mathrm{Pr}}(\tilde{\mu}_{\mathrm{DH}}\tilde{T}_{\tilde{Y}_{\mathrm{DH}}})_{\tilde{Y}_{\mathrm{DH}}} = 0, \tag{23c,d}$$

where

$$\tilde{\mu}_{\mathrm{DH}} = \tilde{\mu}/\tilde{T} = \frac{(T_w + \bar{C})\tilde{T}^{1/2}}{T_w\tilde{T} + \bar{C}}. \tag{24}$$

The boundary and matching conditions read

$$\tilde{U}(\tilde{X}, 0) = \tilde{V}_{\mathrm{DH}}(\tilde{X}, 0) = 0, \quad \tilde{T}(\tilde{X}, 0) = 1 + \Theta_m f(\tilde{X}), \tag{25a,b,c}$$

$$\tilde{U} \to \tilde{Y}_{\mathrm{DH}} + I_{T0} + \tilde{A}, \quad \tilde{T} \to 1 \quad \text{as } \tilde{Y}_{\mathrm{DH}} \to \infty, \tag{26a,b}$$

where

$$I_{T0} = \int_0^\infty (\tilde{T} - 1) d\tilde{Y}_{\mathrm{DH}} = \int_0^\infty (1 - \tilde{T}^{-1}) d\tilde{Y}. \tag{27}$$

This system Eq. (23) is closer to the incompressible lower-deck equation system as in Ref. [20], but we still have the impact of the temperature in the pressure-gradient and viscous terms of the momentum equation. Comparing the matching condition Eq. (26a) with that for the roughness configuration (Eq. (B9) in Ref. [20]), we find that the impact of the temperature distortion I_{T0} is equivalent to that of the shape function of the roughness by producing a displacement effect to the main deck.

3. *Upper deck*

The lower-deck equations are not closed, and an additional pressure-displacement (P-D) relation is obtained by matching the lower-deck solution with the upper-deck solution through the main-deck one. The upper deck has a thickness of $y \sim \epsilon^{-1}$, and its governing equation in a supersonic flow is a rescaled Helmholtz equation, whose solution follows two characteristic curves, and only the radiating branch satisfies the physical situation of the mean flow distorted by the HCS. Applying the transverse momentum equation at the lower boundary, we can obtain the P-D relation [49],

$$\tilde{P}(\tilde{X}) = -\tilde{A}_{\tilde{X}}(\tilde{X}). \tag{28}$$

The nonlinear system Eq. (23) with boundary and matching conditions Eqs. (25) and (26), and the P-D relation Eq. (28) are to be solved numerically. The detailed numerical method is introduced in Appendix A 1. In the limit of $\Theta_m \ll 1$, the system can be solved analytically, which is similar to Ref. [42].

4. *A composite solution*

The mean flow in the boundary layer can be expressed in terms of a composite solution,

$$u = U_B + \epsilon U_{B,y} A + \epsilon \mathcal{R}_u^{-1}(\tilde{U} - \tilde{Y} - \tilde{A}) + \cdots, \qquad T = T_B + T_w(\tilde{T} - 1) + \epsilon T_{B,y} A + \cdots. \tag{29a,b}$$

B. Perturbation field

Being different from subsonic boundary layers, the supersonic boundary layers could support a multiplicity of instability modes [2]. The first modes with oblique angles greater than $\tan^{-1}\sqrt{M^2 - 1}$ belong to the viscous nature [50], while the other modes belong to the inviscid nature, which are driven by the generalized inflectional point of the base flow. In the asymptotic framework, the viscous mode is described by the classical triple-deck structure [51], whereas the inviscid mode is described by a double-layered structure, a main layer where $y = O(1)$ and a Stokes layer where $y = O(R^{-1/2})$. In this paper, we only focus on the inviscid mode.

1. *Main layer*

According to Refs. [13,20], the inviscid Mack mode in the main layer can be described by the Rayleigh equation, and therefore, we introduce $\hat{\phi} = (\hat{v}, \hat{p})^T$ as the eigenfunction of the eigenvalue system. If the HCS is absent, then the main-layer perturbation in the neighborhood of $x = 0$ is expressed as

$$\mathcal{E}[\hat{\phi}(y; x = 0) + \cdots]\, e^{i[\epsilon^{-1}\int \alpha(X)dX + \beta z - \omega t]} + \text{c.c.}, \tag{30}$$

where α, β, ω, and $\mathcal{E}$ denote the streamwise wave number, spanwise wave number, frequency, and amplitude, respectively, and c.c. the complex conjugate. For a spatially evolving mode, ω and β are real, and $\alpha = \alpha_r + i\alpha_i$ is complex with $-\alpha_i$ representing the growth rate. For normalization, we let $\hat{p}(0) = 1$.

As the Mack mode approaches the HCS vicinity, the perturbation is deformed by the mean-flow distortion, which can be expressed in terms of an asymptotic series,

$$\tilde{\phi}(X, y, z, t) = \mathcal{E}(\tilde{\phi}_0 + \epsilon\tilde{\phi}_1 + \cdots)\, e^{i[\epsilon^{-1}\int_{-\infty}^{X} \alpha dX + \beta z - \omega t]} + \text{c.c.} \tag{31}$$

Note that in Ref. [20], the third-order terms, of $O(\epsilon^4\Delta^2)$, were also taken into account, to reveal the impact of the nonparallelism and to match with the outer solutions with a length scale of $O(L/\delta^*)$. Because these terms are much smaller than the low-order terms, we do not show them in this paper for brevity.

Because the mean-flow distortion induced by the HCS varies in a longer length scale than the Mack wavelength, the leading-order perturbation can be expressed as

$$\tilde{\phi}_0(X, y) = C_0(X)\hat{\phi}(y) + \cdots, \tag{32}$$

where $\hat{\phi}$ satisfies the Rayleigh equation,

$$\mathcal{L}_R\hat{\phi} \equiv (\partial_y - \mathbf{H}_0)\hat{\phi} = 0 \quad \text{with} \quad \mathbf{H}_0 = \begin{pmatrix} \frac{U_B'}{U_B - c} & \frac{-M^2 S_0^2 - \tilde{\alpha}^2 T_B}{S_0} \\ -\frac{S_0}{T_B} & 0 \end{pmatrix}, \tag{33}$$

where $S_0 = i\alpha(U_B - c)$, $c \equiv \omega/\alpha$, and $\tilde{\alpha} = \sqrt{\alpha^2 + \beta^2}$. The operator $\mathcal{L}_R \equiv (\partial_y - \mathbf{H}_0)$ is referred to as the Rayleigh operator. It is seen that the viscous terms do not appear in the equations of this order, rendering the inviscid nature of the main layer. Note that Eq. (33) may become singular when c is real, which happens for a neutral mode. Therefore, a viscous critical layer where $U_B = c$ with a thickness of $O(R^{-1/3}\delta)$, must be taken into account. Alternatively, in the numerical process, we can employ a simpler numerical method as in Ref. [13], namely, the integration path around the critical point is detoured by adding a negative imaginary part to y and extending the mean flow to the complex plane.

Equation (33) is subject to the nonpenetration condition at the wall and the attenuation condition in the far-field, namely,

$$\hat{v}(0) = 0; \quad \hat{p}(y) \to 0 \quad \text{as } y \to \infty. \tag{34a,b}$$

Equation (33) with Eq. (34) forms an eigenvalue system, which can be solved numerically using the Malik's approach [52]; a brief introduction can be found in Appendix B.

It should be noted that for a high-M hypersonic boundary layer with an extremely cold wall, the second mode near the upper-branch neutral point is likely to radiate acoustic waves to the far field [53,54]. The condition for the emergence of the radiating mode is that the instability must propagate supersonically with respect to the freestream velocity, namely, the phase speed is slower than the slow-acoustic speed $1 - 1/M$ or faster than the fast-acoustic speed $1 + 1/M$. For the radiating mode, the nonpenetration condition Eq. (34a) is still valid, but the attenuation condition Eq. (34b) must be changed to an oscillatory one to represent the radiated acoustic waves, i.e.,

$$\hat{p}(y) \sim e^{i k_y y} \quad \text{as } y \to \infty, \tag{35}$$

where the complex wall-normal wave number k_y is given by $k_y = -[M^2(\alpha - \omega)^2 - \tilde{\alpha}^2]^{1/2}$. Here the minus sign on the right-hand side is selected to ensure the wave is outgoing, namely, $(d\omega/dk_y)_r > 0$. Thus, if $c_r < 1 - 1/M$, the upper boundary condition Eq. (34b) should be replaced by

$$\hat{p}' = i k_y \hat{p} \quad \text{as } y \to \infty. \tag{36}$$

Because the main-layer solution of the perturbation does not lead to any singularity in the lower deck, it directly matches with the Stokes-layer solution to satisfy the no-slip condition at the wall. Analysis to be shown in Sec. III B 3 reveals that an outflux of $O(\epsilon^2)$ is produced from the Stokes layer. As pointed out by Refs. [13,20], the accuracy of the Rayleigh solution could be improved remarkably if this $O(\epsilon^2)$ correction is taken into account, which leads to an improved boundary condition for Eq. (34a),

$$\hat{v}(0) = -\epsilon^2 \mathcal{C}\hat{p}(0), \quad \mathcal{C} = C_w^{1/2}\left[\frac{i(\gamma - 1)\omega M^2}{(-i\omega \mathrm{Pr})^{1/2}} + \frac{\tilde{\alpha}^2 T_w}{(-i\omega)^{3/2}}\right], \tag{37}$$

where $-i \equiv e^{3\pi i/2}$ and $C_w = \mu_w T_w$. This correction can be also obtained from the Stokes-layer analysis Eq. (56) (taking a case without any HCS). Because the parameter $\mathcal{C}$ in Eq. (37) is practically large for high Mach numbers and wall temperatures, the improved boundary condition renders a more precise prediction of the dispersion relation of the Mack instability especially in the hypersonic regime. The system Eq. (33) with Eqs. (37) and (34b) can be rewritten by

$$\bar{\mathcal{L}}_R\hat{\boldsymbol{\psi}} \equiv (\partial_y - \bar{\mathbf{H}}_0)\hat{\boldsymbol{\psi}} = 0, \quad \text{with } \hat{\psi}_{(1)}(0) = 0 \quad \hat{\psi}_{(2)}(\infty) \to 0, \tag{38}$$

where $\hat{\boldsymbol{\psi}} = (\hat{\psi}_{(1)}, \hat{\psi}_{(2)})^T \equiv (\hat{v} + \epsilon^2 \mathcal{C}\hat{p}, \hat{p})^T$, and

$$\bar{\mathbf{H}}_0 = \begin{pmatrix} \{\mathbf{H}_0\}_{11} + \epsilon^2 \mathcal{C}\{\mathbf{H}_0\}_{21} & \{\mathbf{H}_0\}_{12} - \epsilon^2 \mathcal{C}(\{\mathbf{H}_0\}_{11} + \epsilon^2 \mathcal{C}\{\mathbf{H}_0\}_{21}) \\ \{\mathbf{H}_0\}_{21} & -\epsilon^2 \mathcal{C}\{\mathbf{H}_0\}_{21} \end{pmatrix}. \tag{39}$$

Substituting Eq. (30) with Eqs. (31) and (32) into Eq. (2) and retaining the $O(\mathcal{E}\epsilon)$ terms, we obtain the governing equations for the second-order perturbations, $\tilde{\boldsymbol{\psi}}_1 \equiv (\tilde{v}_1 + \epsilon^2 \mathcal{C}\tilde{p}_1, \tilde{p}_1)^T$,

$$\bar{\mathcal{L}}_R \tilde{\boldsymbol{\psi}}_1 = -i \frac{\partial \bar{\mathbf{H}}_0}{\partial \alpha} C_0'(X)\hat{\boldsymbol{\psi}} + \bar{\mathbf{H}}_1 A(X) C_0(X)\hat{\boldsymbol{\psi}}, \tag{40}$$

where $\bar{\mathbf{H}}_1 = d\bar{\mathbf{H}}_0/dy$. Matching with the lower-deck perturbation as will be shown in Sec. III B 2, we obtain the boundary conditions for the second-order perturbations,

$$\tilde{v}_1(X,0) = -I_1(X) C_0(X)\hat{v}_y(0), \quad \tilde{p}_1(X,\infty) \to 0, \tag{41a,b}$$

where, from Eq. (58) (to be introduced in Sec. III B 3), $I_1(X) = (\mathscr{H}_1 I_{T1}(X) - \epsilon \mathscr{H}_2 I_{C1}(X) + \epsilon \mathscr{H}_3 I_{f1}(X))$, with

$$\mathscr{H}_1 = \frac{1}{\omega^2 M^2/(\tilde{\alpha}^2 T_w) - 1}, \quad \mathscr{H}_2 = \frac{i\omega\mathcal{C}}{\tilde{\alpha}^2 T_w}\mathscr{H}_1 \quad \mathscr{H}_3 = (-i\omega)^{-1/2} C_w^{1/2} \mathscr{H}_1, \tag{42}$$

$$I_{T1} = \int_0^\infty (\tilde{T} - 1)dY = \mathcal{R}_Y^{-1}\tilde{I}_{T1} \equiv \mathcal{R}_Y^{-1}\int_0^\infty (\tilde{T} - 1)d\tilde{Y}, \quad I_{C1} = C_{00}^{1/2} - 1, \quad I_{f1} = C_{00}^{1/2}\Theta_m f, \tag{43}$$

$C_{00}(X) = \tilde{\mu}(X,0)\tilde{T}(X,0)$. Therefore, the regularized boundary conditions for Eq. (40) read

$$(\tilde{\psi}_1)_{(1)}(X,0) = -I_1(X) C_0(X)\hat{v}_y(0), \quad (\tilde{\psi}_1)_{(2)}(X,\infty) \to 0. \tag{44a,b}$$

For a radiating mode, Eq. (44b) is replaced by $(\psi_1)_{(2),y}(X,\infty) = i k_y (\psi_1)_{(2)}(X,\infty)$.

Following a standard treatment as in Refs. [55,56], the system Eq. (40) with boundary conditions Eq. (44) can be recast to

$$\bar{\mathcal{L}}_R \tilde{\boldsymbol{\psi}}_1 = -i \frac{\partial \bar{\mathbf{H}}_0}{\partial \alpha} C_0'(X)\hat{\boldsymbol{\psi}} + \bar{\mathbf{H}}_1 A(X) C_0(X)\hat{\boldsymbol{\psi}} + I_1 C_0(X)\delta(y)\mathbf{D}, \tag{45}$$

$$(\tilde{\psi}_1)_{(1)}(X,0) = 0, \quad (\tilde{\psi}_1)_{(2)}(X,y) \to 0 \; [\text{or } (\tilde{\psi}_1)_{(2),y} = i k_y (\tilde{\psi}_1)_{(2)}] \quad \text{as } y \to \infty, \tag{46}$$

where δ is the Dirac δ function, and $\mathbf{D} = [-\hat{\psi}_{(1)}'(0), 0]^T$.

2. Lower deck

Now we consider the lower deck where $Y = O(1)$, the analysis of which determines the outflux velocity as in Eq. (41a). Applying Eq. (31) at the bottom of the main layer, and taking into account the linearized N-S equations, we can estimate the magnitudes of the perturbations in the lower deck,

$$(\tilde{u}, \tilde{v}, \tilde{w}, \tilde{\rho}, \tilde{\theta}, \tilde{p}) = \mathcal{E}(\bar{u}_0, \epsilon\bar{v}_0, \bar{w}_0, \bar{\rho}_0, \bar{\theta}_0, \bar{p}_0)\, e^{-i(\beta z - \omega t)} + \cdots + \text{c.c.} \tag{47}$$

Substitute of the mean flow Eq. (14) with the perturbations Eq. (47) into the N-S equations, we obtain

$$-i\omega\bar{\rho}_0 + \frac{\tilde{R}}{T_w}(\bar{u}_{0,x} + \bar{v}_{0,Y} + i\beta\bar{w}_0) + \frac{\tilde{R}_Y}{T_w}\bar{v}_0 = 0, \quad -i\omega\frac{\tilde{R}}{T_w}\bar{u}_0 = -\bar{p}_{0,x}, \tag{48a,b}$$

$$\bar{p}_{0,Y} = 0, \quad -i\omega\frac{\tilde{R}}{T_w}\bar{w}_0 = -i\beta\bar{p}_0, \tag{48c,d}$$

$$\frac{\tilde{R}}{T_w}(-i\omega\bar{\theta}_0 + T_w\tilde{T}_Y\bar{v}_0) = -i\omega(\gamma - 1)M^2\bar{p}_0, \quad T_w\tilde{T}\bar{\rho}_0 + \frac{\bar{\theta}_0}{T_w\tilde{T}} = \gamma M^2\bar{p}_0. \tag{48e,f}$$

Note that $\tilde{R}$ is a function of $\tilde{X}$ (or X) and $\tilde{Y}$, and the perturbation in this layer is inviscid to leading-order accuracy. Matching with the main-layer solution Eq. (31), it is found that

$$\bar{p}_0 = C_0(X)\, e^{i\epsilon^{-1}\int_{-\infty}^{X}\alpha dX}\, \hat{p}(0) = C_0(X)\, e^{i\int_{-\infty}^{x}\alpha dx}\, \hat{p}(0). \tag{49}$$

The dependence of $\bar{p}_0$ on the streamwise coordinate separates into two scales, $O(1)$ and $O(\epsilon)$. Solving Eq. (48), we obtain, to leading-order accuracy,

$$(\bar{u}_0, \bar{w}_0, \bar{v}_0) = \Big(\frac{\alpha T_w \tilde{T}}{\omega}, \frac{\beta T_w \tilde{T}}{\omega}, i\omega M^2 Y - \frac{i\tilde{\alpha}^2 T_w}{\omega}\int_0^Y \tilde{T}\, dY + \epsilon \bar{v}_{01}\Big)\bar{p}_0, \tag{50a,b,c}$$

$$\tilde{\theta}_0 = (\gamma-1)M^2 T_w \tilde{T}\, \bar{p}_0 - \frac{i\tilde{T}_Y T_w}{\omega}\bar{v}_0, \quad \bar{\rho}_0 = \frac{M^2 \bar{p}_0}{T_w \tilde{T}} + \frac{i\tilde{T}_Y \bar{v}_0}{\omega T_w \tilde{T}^2}, \tag{50d,e}$$

where $\epsilon\bar{v}_{01}$ is the outflux from the Stokes layer. Because the thickness of the Stokes layer is of $O(\epsilon^2)$, we can estimate that the order of magnitude of this term is $O(\epsilon)$. Since the outflux is rather small, the Stokes-layer perturbations plays a secondary role on the scattering process. We perform the analysis of the Stokes layer is only for completeness, and in the numerical calculations in Sec. V, the $O(\epsilon)$ terms will not be considered.

As $\tilde{Y} \to \infty$, the transverse velocity perturbation behaves as

$$\bar{v}_0 \to \left[\left(i\omega M^2 - \frac{i\tilde{\alpha}^2 T_w}{\omega}\right)Y - \frac{i\tilde{\alpha}^2 T_w}{\omega} I_{T1} + \epsilon\bar{v}_{01}\right]\bar{p}_0. \tag{51}$$

From Eq. (50) we know that

$$(\bar{u}_0, \bar{w}_0, \bar{\theta}_0) \to \left[\frac{\alpha}{\omega}, \frac{\beta}{\omega}, (\gamma-1)M^2\right] T_w[1+\Theta_m f(X)]\bar{p}_0 \quad \text{as } \tilde{Y} \to 0. \tag{52}$$

Obviously, these solutions do not satisfy the no-slip and isothermal conditions, and so a Stokes layer needs to be taken into account.

3. Stokes layer

In the Stokes layer where $y \sim \epsilon^2$, we introduce a local coordinate

$$Y_S = \epsilon^{-2} y. \tag{53}$$

Following Ref. [13], we obtain the Stokes-layer solutions

$$(\tilde{u}, \tilde{w}) = \left(\frac{\alpha}{\omega}, \frac{\beta}{\omega}\right)\left[1 - \exp\left(\left(\frac{-i\omega}{C_w C_{00}}\right)^{1/2} Y_S\right)\right] T_w[1+\Theta_m f(X)]\bar{p}_0 + \cdots, \tag{54a,b}$$

$$\tilde{\theta} = (\gamma-1)M^2\left[1 - \exp\left(\left(\frac{-i\omega \mathrm{Pr}}{C_w C_{00}}\right)^{1/2} Y_S\right)\right] T_w[1+\Theta_m f(X)]\bar{p}_0 + \cdots. \tag{54c}$$

Such solutions guarantee the validation of the wall boundary conditions.

Integrating the continuity equation in the Stokes layer, we obtain the transpiration velocity

$$\begin{aligned}\tilde{v} = \epsilon^2\Bigg[\left(i\omega M^2 + \frac{\tilde{\alpha}^2 T_w(1+\Theta_m f)}{i\omega}\right)Y_S - \frac{i(\gamma-1)(C_w C_{00})^{1/2}\omega M^2}{(-i\omega \mathrm{Pr})^{1/2}}\big(1 - e^{(\frac{-i\omega \mathrm{Pr}}{C_w C_{00}})^{1/2} Y_S}\big) \\ - \frac{\tilde{\alpha}^2 (C_w C_{00})^{1/2} T_w (1+\Theta_m f)}{(-i\omega)^{3/2}}\big(1 - e^{(\frac{-i\omega}{C_w C_{00}})^{1/2} Y_S}\big)\Bigg]\bar{p}_0.\end{aligned} \tag{55}$$

In the limit of $Y_S \to \infty$,

$$\tilde{v} \to \epsilon^2\left[\left(i\omega M^2 + \frac{\tilde{\alpha}^2 T_w(1+\Theta_m f)}{i\omega}\right)Y_S - (C_w C_{00})^{1/2}\left(\frac{i(\gamma-1)\omega M^2}{(-i\omega \mathrm{Pr})^{1/2}} + \frac{\tilde{\alpha}^2 T_w(1+\Theta_m f)}{(-i\omega)^{3/2}}\right)\right]\bar{p}_0. \tag{56}$$

Therefore, an outflux $\epsilon\hat{v}_{10}$ [defined in Eq. (50c)] is induced to the lower deck, where

$$\hat{v}_{10} = \left[-\mathcal{C}\big(C_{00}^{1/2} - 1\big) - (C_w C_{00})^{1/2}\frac{\tilde{\alpha}^2 T_w \Theta_m f}{(-i\omega)^{3/2}} \right]\bar{p}_0. \tag{57}$$

Combining Eqs. (51) and (57), we obtain the wall boundary condition of the main-layer transverse velocity,

$$\tilde{v}_1(X,0) = -\mathscr{H}_1\left[I_{T1} - \epsilon\left(\frac{i\omega\mathcal{C}I_{C1}}{\tilde{\alpha}^2 T_w} + (-i\omega)^{-1/2}C_w^{1/2}I_{f1} \right)\right] C_0(X)\hat{v}_y(0), \tag{58}$$

where $\bar{p}_0(0)$ has been converted to $\bar{v}_y(0)$ through the Rayleigh equation at the wall. Thus, we obtain the boundary condition for $\tilde{v}_1$ in Eq. (44).

It should be mentioned that for a case without any HCS, for which $C_{00} = 1$ and $\Theta_m = 0$, the second term on the right-hand side of Eq. (56) determines the $O(\epsilon^2)$ outflux from the Stokes layer to the main layer, leading to the improved boundary condition Eq. (37).

C. Amplitude equation and transmission coefficient

In this subsection, we will consider the evolution of the amplitude of the oncoming Mack mode, whose interaction with the HCS is characterized by a transmission coefficient $\mathscr{T}$. Following Ref. [14], the transmission coefficient is defined as the ratio of the Mack amplitude downstream of the HCS to that upstream, such that the shift of the transition onset is explicitly determined by the asymptotic model.

Introduce the adjoint vector of the Rayleigh equation, $\hat{\boldsymbol{\psi}}^\dagger = (\hat{\boldsymbol{\psi}}^\dagger_{(1)}, \hat{\boldsymbol{\psi}}^\dagger_{(2)})^T$, which satisfies

$$\big(\partial_y + \bar{\mathbf{H}}_0^T\big)\hat{\boldsymbol{\psi}}^\dagger = 0, \quad \text{with } \hat{\boldsymbol{\psi}}^\dagger_{(2)}(0) = 0, \quad \hat{\boldsymbol{\psi}}^\dagger_{(1)}(y) \to 0 \quad \text{as} y \to \infty. \tag{59a,b,c}$$

Again, for a radiating mode, Eq. (59c) is replaced by $\hat{\boldsymbol{\psi}}^\dagger_{(1),y} = i k_y \hat{\boldsymbol{\psi}}^\dagger_{(1)}$ as $y \to \infty$. For normalization, we let $\hat{\boldsymbol{\psi}}^\dagger_{(1)}(0) = 1$.

The system Eq. (45) with the boundary condition Eq. (46) has nontrivial solutions only if the right-hand side of Eq. (45) is orthogonal to the adjoint vector $\hat{\boldsymbol{\psi}}^\dagger$ (solvability condition). This leads to the amplitude equation,

$$iC_0'(X) = [A(X)K_0 + I_1(X)K_1]C_0(X), \tag{60}$$

where the efficiency functions are

$$K_0 = \frac{\langle \hat{\boldsymbol{\phi}}^\dagger, \bar{\mathbf{H}}_1\hat{\boldsymbol{\phi}}\rangle}{\langle \hat{\boldsymbol{\phi}}^\dagger, (\partial\bar{\mathbf{H}}_0/\partial\alpha)\hat{\boldsymbol{\phi}}\rangle}, \quad K_1 = \frac{\langle \hat{\boldsymbol{\phi}}^\dagger, \delta(y)\mathbf{D}\rangle}{\langle \hat{\boldsymbol{\phi}}^\dagger, (\partial\bar{\mathbf{H}}_0/\partial\alpha)\hat{\boldsymbol{\phi}}\rangle}, \tag{61a,b}$$

$$\langle \boldsymbol{\phi}^\dagger, \boldsymbol{\phi}\rangle \equiv \int_0^\infty (\boldsymbol{\phi}^\dagger)^T \boldsymbol{\phi}\, dy \tag{62}$$

denotes the inner product. Here AK_0 represents the effect of the main-layer mean-flow distortion, where the strength of the mean-flow distortion A and the instability property K_0 are readily separated; I_1K_1 is induced by the effect of the HCS on the Mack mode from the underneath lower and Stokes layers. From Ref. [20] we know that $K_0 = K_1$.

Because the impact of the HCS in the upstream limit is exponentially small, we put

$$C_0(X) \to 1 \quad \text{as } X \to -\infty. \tag{63}$$

Solving the amplitude Eq. (60) subject to Eq. (63), we obtain

$$C_0(X) = \exp\left[-iK_0\int_{-\infty}^{X} (A(X) + I_1(X))dX \right]. \tag{64}$$

The transmission coefficient $\mathscr{T}$ can be evaluated by the behavior of C_0 in the downstream limit, which is essentially an integral of A and I_1 from $-\infty$ to ∞. This treatment has been used in Ref. [20]. However, we may face a difficulty in the present circumstance. It can be inferred from Ref. [40] that for low roughness, the displacement function A decays like $X^{-5/3}$ in the downstream limit, implying that the integral of A to infinity is bounded. However, the displacement function for a linear HCS ($\Theta_m \ll 1$) decays like

$$A \sim X^{-2/3} \quad \text{as} \;\; X \to \infty, \tag{65}$$

as shown in Ref. [42], leading to an unbounded value of $\int_{-\infty}^{\infty} A dX$. Note that such a scaling was obtained by assuming $\Theta_m \ll 1$, but as will be confirmed numerically in Fig. 3(b), it also holds when $\Theta = O(1)$. The implication is that it is not possible to obtain a convergent transmission coefficient for a HCS-induced scattering problem. There may be two ways to overcome this shortcoming:

(1) The first way is to interpret $\int_{-\infty}^{\infty} A dX$ in the sense of Hadamard finite-part integral as in Ref. [14]. Let us denote

$$J_\infty = \int_{-\infty}^{\infty} A dX = \int_{-\infty}^{N_0} A dX + \int_{N_0}^{\infty} A dX \approx \int_{-\infty}^{N_0} A dX - 3A_\infty N_0^{1/3}, \tag{66}$$

where N_0 is a sufficiently large value such that the asymptote of $A(X)$ for $X > N_0$ is arrived, namely,

$$A(X) \approx A_\infty X^{-2/3} + O(X^{-5/3}) \quad \text{for} \;\; X \geqslant N_0. \tag{67}$$

It can be proved that $\partial J_\infty / \partial N_0$ is zero to leading order, indicating that the choice of N_0 does not affect the whole integral; a numerical proof can be seen in Appendix A of Ref. [14].

(2) The second way is to truncate the integral at some finite X_N. We define the transmission coefficient as

$$\mathscr{T} \equiv C_0(X_N) = \exp[-i K_0(\mathcal{D}_1 + \mathscr{H}_1 \mathcal{D}_2 - \epsilon \mathscr{H}_2 \mathcal{D}_3 + \epsilon \mathscr{H}_3 \mathcal{D}_4)], \tag{68}$$

where

$$\mathcal{D}_1 = \int_{-\infty}^{X_N} A dX, \quad \mathcal{D}_2 = \int_{-\infty}^{X_N} I_{T1} dX, \quad \mathcal{D}_3 = \int_{-\infty}^{X_N} I_{C1} dX, \quad \mathcal{D}_4 = \int_{-\infty}^{X_N} I_{f1} dX. \tag{69a,b,c,d}$$

In this sense, $\mathscr{T}$ is dependent on the location of X_N. Because we are going to compare our theoretical predictions with the HLNS calculations, a fair comparison should be made by measuring the transmission coefficient at the same location. Therefore, we choose $X_N = \epsilon x_N$, where x_N is a sufficiently downstream location for the HLNS calculation. In this paper, we choose $x_N = 50$, where the asymptote Eq. (65) has been reached; a detailed discussion will be provided in Sec. V C 2.

Comparing Eq. (66) with Eq. (78a), we find that J_∞ and $\mathcal{D}_1$ are differed by $-3A_\infty X_N^{1/3}$, which is the infinite part of the integral as $X_N \to \infty$. The implication is that the two ways represent two different physical meanings. The first way ignores the infinite part of the integral and provides a convergent integral in the ideally downstream limit, however, since the laminar state will eventually transition to turbulence, the ideal downstream phase is not related to the physical situation. Since the displacement function does not change its sign for any X, its accumulation ($\mathcal{D}_1$) increases monotonically as X_N increases. From the physical point of view, such an accumulation indeed leads to a gradual change of the transmission coefficient with X_N, and therefore, the second way is employed for the following calculations.

Considering that the terms $\epsilon \mathscr{H}_2 \mathcal{D}_3$ and $\epsilon \mathscr{H}_3 \mathcal{D}_4$, both of which are of $O(\epsilon)$, are quantitatively small, Eq. (68) can be simplified as

$$\mathscr{T} = \exp[-i K_0(\mathcal{D}_1 + \mathscr{H}_1 \mathcal{D}_2)]. \tag{70}$$

It is also confirmed numerically that the effect of the $O(\epsilon)$ terms are negligible.

Let us revisit the transmission coefficient for roughness cases introduced in Eq. (2.32) of Ref. [20], which reads $\mathscr{T} = \exp[-i K_0(\mathcal{D}_1 + h\mathcal{D}_2)]$, where h is the height of the roughness and

$\mathcal{D}_2$ is an integral of the surface shape function of the roughness. In such an expression, the impact of the instability property, K_0, and that of the mean-flow distortion, $\mathcal{D}_1$ and $h\mathcal{D}_2$, are readily separated. However, for the cases of HCSs, a prefactor $\mathscr{H}_1$, associated with the instability property, appears in front of the term $\mathcal{D}_2$, leading to a more complicated dependence of $\mathscr{T}$ on the two factors. $\mathscr{H}_1\mathcal{D}_2$ appears in the same place as $h\mathcal{D}_2$ in the roughness configuration, indicating that the HCS can play an equivalent role as the roughness, and $\mathscr{H}_1 I_{T1}$ is quantitatively equivalent to the geometric function of the surface roughness.

IV. DNS AND HLNS APPROACHES

A. DNS approach

Alternatively, one can re-express the full N-S Eqs. (2) in terms of the conservative form [57] and solve the nonlinear equation system directly by numerical schemes, which is referred to as DNS. The DNS code in this paper is the same as that used in Refs. [19,20,31].

The calculations include two steps. First, one needs to calculate the steady mean flow distorted by the surface HCS, $\bar{\boldsymbol{\varphi}}$ in Eq. (4). For a 2D HCS, we choose a rectangular computational domain $[x_0, x_I] \times [0, y_J]$. $I + 1$ and $J + 1$ nonuniform grid points that are clustered near the HCS and the wall are used in the streamwise and wall-normal directions, respectively. Each grid point is labeled by (i, j) with $i \in [0, I]$ and $j \in [0, J]$. The convective and viscous terms are discretized by the fifth-order partial and fourth-order central finite difference schemes, respectively, and the third-order Runge-Kutta method is used for time advancing. At the inlet of the computational domain, x_0, the Blasius solution is introduced because the impact of the HCS is somewhat local. The no-slip, nonpenetration and isothermal conditions are imposed at the wall, $y = 0$. A buffer region is introduced near the outlet $x \in [x_I, x_I + \Delta_{\text{buffer}}]$ with Δ_{buffer} denoting the length of the buffer region, and the outflow condition is used at the upper boundary y_J. The calculation is carried out until the solution converges to a time-independent state.

Second, we calculate the unsteady perturbation field $\tilde{\boldsymbol{\varphi}}$ in the selected domain. If the perturbation is 3D, then we need to introduce a spanwise coordinate z and extend the mean flow such that it is uniform in the z direction. The numerical approach is exactly the same as that of the first step except for the inflow condition, which is changed to the sum of a steady mean flow and a harmonic Mack mode with an infinitesimal amplitude,

$$\boldsymbol{\varphi}(x_0, y, z, t) = \bar{\boldsymbol{\varphi}}(x_0, y) + \tilde{\boldsymbol{\varphi}}(x_0, y, z, t). \tag{71}$$

For a position sufficiently upstream of the HCS, where the nonparallelism of the base flow is rather weak, the second term on the right-hand side of Eq. (71) is further expressed as

$$\tilde{\boldsymbol{\varphi}}(x, y, z, t) = \mathcal{E}\hat{\boldsymbol{\varphi}}(y; x_0)\, e^{i(\int_{x_0}^{x} \alpha dx + \beta z - \omega t)} + \text{c.c.}, \tag{72}$$

where $\hat{\boldsymbol{\varphi}}(y; x_0)$ is the perturbation profile at $x = x_0$, and the amplitude $\mathcal{E}$ is taken to be 10^{-8}. The complex wave number α and the perturbation profile $\hat{\boldsymbol{\varphi}}$ are the eigenvalue and eigenfunction of compressible O-S equations

$$\mathbf{A}(\alpha; \bar{\boldsymbol{\varphi}}, \omega, \beta, R, M)\hat{\boldsymbol{\varphi}} = 0, \tag{73}$$

where the coefficient matrix $\mathbf{A}$ can be found in Ref. [52].

In this paper, we choose $x_0 = -40$, $x_I = 110$, $y_J = 100$, $I = 1600$, $J = 300$ and $\Delta_{\text{buffer}} = 63$, and 200 grid points are assigned in the buffer region. After obtaining the perturbation field, we calculate the transmission coefficient using

$$\mathscr{T} = \frac{\max_y\{\max_{t>t_0}[\tilde{T}(x_N, y, t_0)]\}_{\text{with}-\text{HCS}}}{\max_y\{\max_{t>t_0}[\tilde{T}(x_N, y, t_0)]\}_{\text{without}-\text{HCS}}}, \tag{74}$$

where t_0 is a time instant after which the perturbation field is statistically steady. In our calculations, we choose $t_0 = 150\pi/\omega$. As mentioned in Sec. III C, we select $x_N = 50$.

B. HLNS approach

If the mean flow has been obtained by the first step of Sec. IV A, then we can calculate the perturbation evolution (the second step) in a more efficient manner. As in Ref. [19], an infinitesimal perturbation can be expressed as

$$\tilde{\boldsymbol{\varphi}} = \mathcal{E}\check{\boldsymbol{\varphi}}(x, y)\, e^{i\alpha_0 x}\, e^{i(\beta z-\omega t)} + \text{c.c.}, \tag{75}$$

where α_0 is a reference complex wave number introduced for convenience of numerics. α_0 is simply selected as the eigenvalue solution of the compressible O-S equations at the inlet $x = x_0$. In contrast to Eq. (72), Eq. (75) describes the perturbation in the whole computational domain, including that near the HCS. Substituting Eq. (75) into the N-S equation system and neglecting the $O(\mathcal{E}^2)$ terms, we obtain a linear system,

$$(\tilde{\mathbf{D}} + \tilde{\mathbf{A}}\partial_x + \tilde{\mathbf{B}}\partial_y + \mathbf{V}_{xx}\partial_{xx} + \mathbf{V}_{yy}\partial_{yy} + \mathbf{V}_{xy}\partial_{xy})\check{\boldsymbol{\varphi}}(x, y) = 0, \tag{76}$$

where the coefficient matrices $\tilde{\mathbf{D}}$, $\tilde{\mathbf{A}}$, $\tilde{\mathbf{B}}$, $\mathbf{V}_{xx}$, $\mathbf{V}_{yy}$, and $\mathbf{V}_{xy}$ can be found in the Appendix of Ref. [19]. Under a proper discretization, the linear system Eq. (76) is reduced to a system of algebraic equations, $\mathbf{M}\tilde{\boldsymbol{q}} = \tilde{\boldsymbol{r}}$, where the coefficient matrices $\tilde{\mathbf{M}}$, the unknown vector $\tilde{\boldsymbol{q}}$ and the inhomogeneous forcing $\tilde{\boldsymbol{r}}$ were illustrated in Ref. [19].

In the HLNS calculation, the computational domain is the same as that in Sec. IV A, and 801 × 301 grid points are employed, which is only a half of those used in DNS. Careful resolution studies have been carried out. The transmission coefficient now is defined as

$$\mathscr{T} = \frac{\max_y[|\check{T}(x_N, y)|]_{\text{with HCS}}}{\max_y[|\check{T}(x_N, y)|]_{\text{without HCS}}}. \tag{77}$$

V. NUMERICAL RESULTS

A. Oncoming conditions and instability of the base flow

A number of case studies with different M, T_w and T_∞ are listed in Table I, in which each case is denoted by a four-character string. The first two characters, “M1” and “M2,” are for $M = 4.5$ and 5.92, respectively. The last two characters distinguish the choices of T_∞ and T_w: “T1(T5),” “T2(T6),” “T3(T7),” and “T4(T8)” are for $T_w/T_{ad} = 1.0$, 0.75, 0.5, and 0.25, respectively, where T_{ad} denotes the adiabatic wall temperature; “T9” is for $T_w/T_{\text{ad}} \approx 0.072$, an extremely cold wall; “T1” to “T4” are for cold oncoming temperatures ($T_\infty = 65.15K$ for M1 and $T_\infty = 48.69K$ for M2; wind tunnel conditions); “T5” to “T9” are for $T_\infty = 226.5$, a flight condition at an altitude of 30 000 m. The shape constant Δ, the nominal boundary-layer thickness δ_{99}, the location of the generalized inflectional point (GIP) y_c and the velocity at the GIP U_c are also shown. Note that the GIPs in cases M1T4, M1T8, and M2T9 disappear. A few representative base-flow profiles can be found elsewhere, such as Refs. [13,20]. Three representative Reynolds numbers for each M are selected. For cases M1T1 to M1T8, we select $R = 50\,000$, 25 000, and 10 000, denoted as R1, R2, and R3, respectively; for cases M2T1 to M2T9, we select R1, R2, and R3 to represent $R = 131\,820$, 65 910, and 26 364, respectively. For instance, a case study with $(M, \text{Re}, T_\infty, T_w) = (4.5, 50\,000, 65.15K, 4.4)$ is denoted by case M1T1R1.

Figure 2 plots the phase speeds c_r and growth rates $-\alpha_i$ of the 2D Mack modes for cases M1T1, M1T4, M2T1, M2T4, and M2T9. The triangles and circles are the solutions of the O-S Eqs. (73) for R1 and R3, respectively, whereas the blue solid and pink dashed lines are the predictions of the improved Rayleigh Eq. (38) for R1 and R3, respectively. Let us first look at the O-S solutions. From the left column, we can see that for each case, two branches of discrete modes emerge from $c_r = 1 - 1/M$ (the slow-acoustic speed) and $1 + 1/M$ (the fast-acoustic speed), respectively, which are referred to as the slow and fast modes, respectively. The curves for different Reynolds numbers almost overlap, indicating a rather weak effect of R on the phase speed. As ω increases, the phase speeds of the two branches approach each other, and intersect at a synchronization frequency ω_s. For the five panels (a, c, e, g, i), $\omega_s \approx 2.0$, 1.15, 1.9, 1.1, and 0.98, respectively. The growth rates,

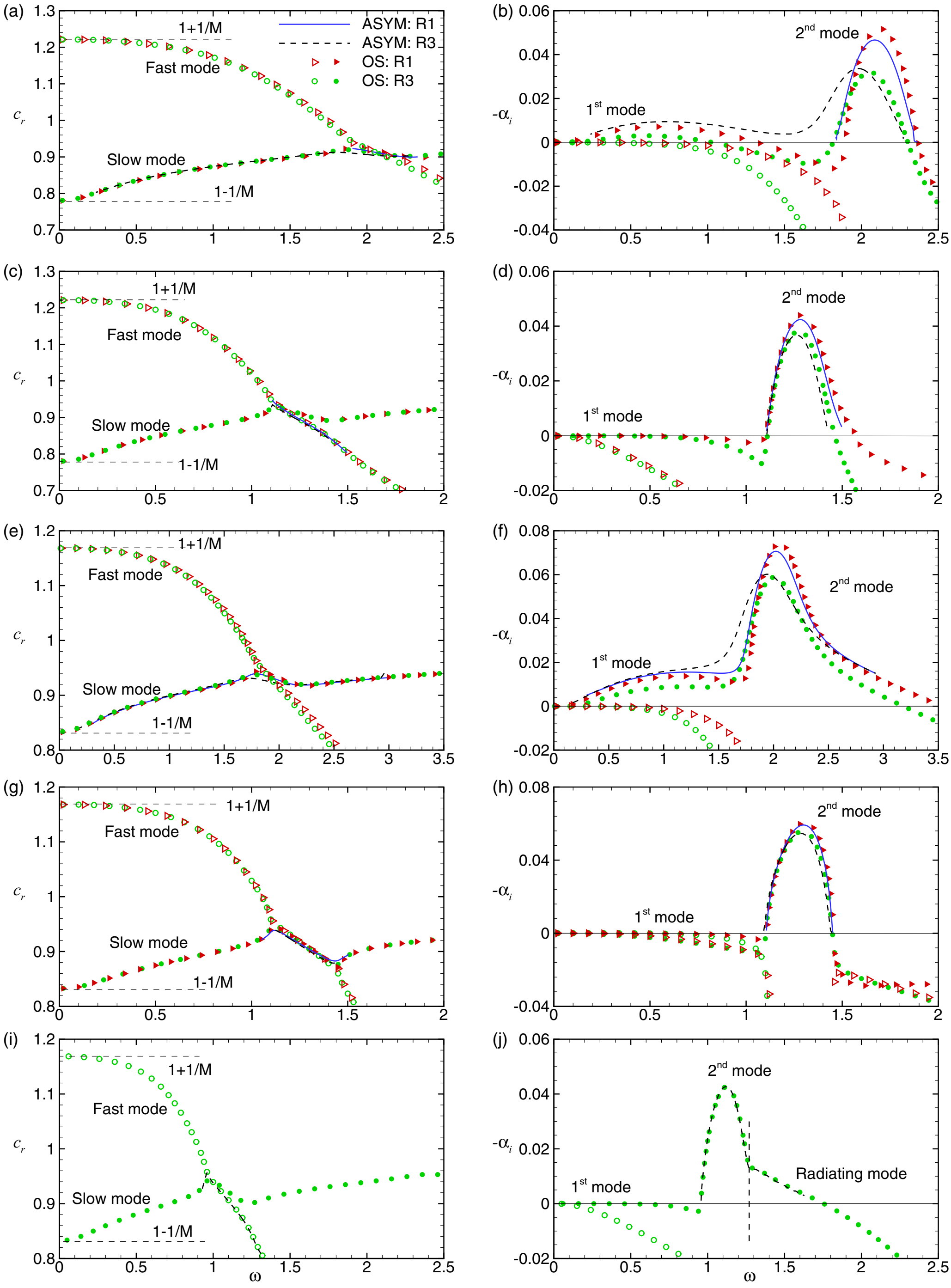

FIG. 2. Dependence on ω of c_r (left column) and $-\alpha_i$ (right column) of the 2D Mack modes, where the velocities of the fast and slow acoustic waves, $1 \pm 1/M$, are marked in the left column. (a), (b) case M1T1; (c), (d) case M1T4; (e), (f) case M2T1; (g), (h) case M2T4; (i), (j) case M2T9. The horizontal lines in the right column represent the zero-growth lines.

as shown in the right column, show overall two unstable regions, which are referred to the first and second modes, respectively. The second modes are more unstable, and for the five panels, the most unstable frequency corresponding to the peaks of the second modes, ω_g, are about 2.1, 1.3, 2.0, 1.3, and 1.1, respectively, slightly greater than ω_s. For the extremely cold wall case, case M2T9R3, a radiating mode emerges when $\omega > 1.27$. Detailed discussion for the radiating mode can be found in Ref. [53].

In Fig. 2, the asymptotic predictions by the improved Rayleigh system Eq. (38) agree quite well with the O-S solutions in the unstable frequency band for most of the cases. Note that for neutral modes, because of the appearance of the viscous critical layer, the eigenfunctions of the Rayleigh equation and its adjoint equation are singular, and so the calculations around the neutral point are difficult and not shown. However, from the physical point of view, we are interested in the scattering of the unstable modes, for which the calculations do not encounter with that difficulty. Appreciable error appears only for cases M1T1R3 and M2T1R3 (adiabatic wall temperature and low Reynolds number), and the discrepancies are restricted in a narrow frequency band around the intersection frequency of the first and second modes.

B. Mean-flow distortion

1. *Solutions in the lower deck of the compressible triple-deck system*

Solving numerically the nonlinear system Eqs. (23)–(28), we obtain the mean-flow distorted by the surface HCS. The verification of the triple-deck calculations is provided in Appendix A 2. Figure 3(a) compares the streamwise evolution of the displacement function $\tilde{A}$ for different Θ_m. For a cooling strip, $\tilde{A}$ is always positive, whereas for a heating strip, $\tilde{A}$ is always negative. This is in contrast to the roughness configuration [20], namely, for both humps and indentations, the displacement function is always negative. For both the heating and cooling strips, the displacement functions approach zero in the upstream limit, and deviate from zero in the HCS vicinity. For the same $|\Theta_m|$, $|\tilde{A}|$ for a cooling strip is slightly greater than that for a heating strip. In the linear regime, $|\Theta_m| \ll 1$, the normalized displacement function, $|\tilde{A}/\Theta_m| = -\tilde{A}/\Theta_m$ must collapse to a single curve. To check the effect of nonlinearity, Fig. 3(b) depicts $-\tilde{A}/\Theta_m$ for different Θ_m. Overall, the nonlinearity is not strong, and the peak of $-\tilde{A}/\Theta_m$ at $\tilde{X} \approx 0$ becomes slightly greater as Θ_m decreases monotonically. The implication is that the nonlinearity leads to a slightly greater distortion for a cooling strip, but a slightly weaker distortion for a heating strip. In the downstream limit, all the curves decay like $\tilde{A} \sim \tilde{X}^{-2/3}$, which agrees with the scaling law predicted by the linear approximation in Ref. [42]. Figure 3(c) shows the streamwise evolution of I_{T1}, which is to be used for the prediction of the transmission coefficient. I_{T1} is positive for $\Theta_m > 0$ and negative for $\Theta_m < 0$, in contrast to $\tilde{A}$. It will be shown in Eq. (6) that $\mathscr{H}_1$ is almost real and positive, thus, from the definition of the transmission coefficient Eq. (70) we know that the opposite sign of I_{T1} and $\tilde{A}$ implies opposite effect of each individual on the scattering process. Again, a cooling strip produces greater mean-flow distortion than a heating strip with the same $|\Theta_m|$. The behavior of I_{T1} in the downstream limit can be estimated as follows. Since $\tilde{A} \sim \tilde{X}^{-2/3}$ in the large-$\tilde{X}$ limit, it is obtained from Eq. (20a) that the mean velocity $\tilde{U} \sim \tilde{Y} + \tilde{X}^{-2/3}\tilde{U}_1$, where $\tilde{U}_1$ is an $O(1)$ function of $\tilde{Y}$. Noting that the compressibility is the leading-order effect, balance of the continuity equation determines that $\tilde{R} \sim 1 + \tilde{X}^{-2/3}\tilde{R}_1$, and thus $\tilde{T} \sim 1 + \tilde{X}^{-2/3}\tilde{T}_1$, where R_1 and T_1 are also $O(1)$ functions of $\tilde{Y}$. Therefore, $\tilde{T} - 1 \sim \tilde{X}^{-2/3}$, so is I_{T1}. The black dot-dot-dashed lines in Fig. 3(c) show the scaling $\tilde{X}^{-2/3}$, which agrees perfectly with the numerical results for large $\tilde{X}$.

2. *Mean-flow distortion for different cases*

It is indicated from Eq. (70) that whether the HCS plays a stabilizing or destabilizing role depends on the combined effect of K_0 and $\mathcal{D}_1 + \mathscr{H}_1\mathcal{D}_2$. Only the latter is associated with the mean-flow distortion. According to Eqs. (10), (21), and (69), we can re-express $\mathcal{D}_1$ and $\mathcal{D}_2$ in terms of the

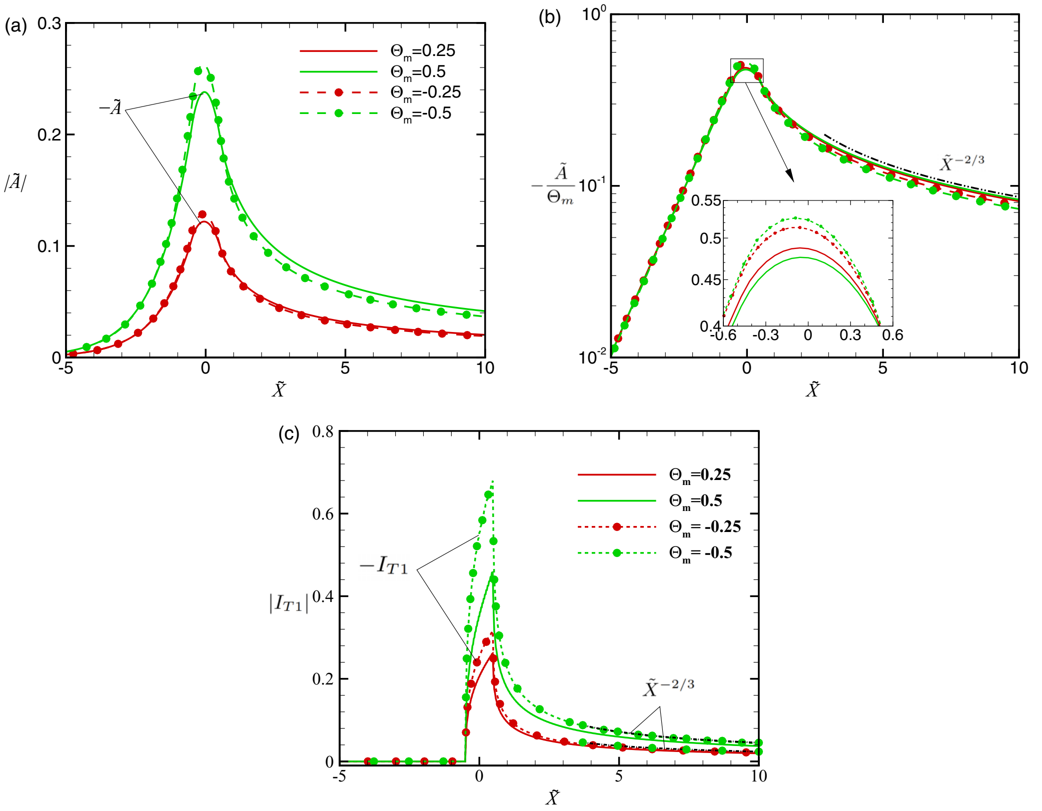

FIG. 3. Streamwise evolution of $|\tilde{A}|$ (a), $-\tilde{A}/\Theta_m$ (b), and $|I_{T1}|$ (c) for $(T_\infty, T_w) = (65.15K, 4.4)$ and $D = 1$ with different Θ_m. For the solid curves in panel (a), $|\tilde{A}| = -\tilde{A}$.

triple-deck variables,

$$\mathcal{D}_1 = \mathcal{R}_Y^{-1}\mathcal{R}_X^{-1}\int_{-\infty}^{X_N}\tilde{A}d\tilde{X}, \quad \mathcal{D}_2 = \mathcal{R}_Y^{-1}\mathcal{R}_X^{-1}\int_{-\infty}^{X_N}\tilde{I}_{T1}d\tilde{X}. \tag{78a,b}$$

Table II lists the calculated $\mathcal{D}_1$ and $\mathcal{D}_2$ for different M, Re, T_∞, T_w, Θ_m, d, and D. Each case is labeled by an eight-character string: the first four characters are from Table I, distinguishing M, T_∞, and T_w; the fifth and sixth characters distinguish the Reynolds numbers, which were defined in Sec. V A; the last two characters distinguish the cases for different HCSs. It is seen that $\mathcal{D}_1$ and $\mathcal{D}_2$ are always with opposite signs, and $\mathcal{D}_1$ is negative (positive) for a heating (cooling) strip. Decrease of T_w leads to monotonic decreases of both $|\mathcal{D}_1|$ and $|\mathcal{D}_2|$, indicating a weaker mean-flow distortion, whereas decrease of T_∞ only leads to a slightly stronger mean-flow distortion. For fixed $(M, T_\infty, T_w, \Theta_m, \frac{d^*}{\delta_{99}})$, $|\mathcal{D}_1|$ and $|\mathcal{D}_2|$ increase as R reduces. As expected, the mean-flow distortion is stronger as $|\Theta_m|$ and/or d increase.

3. Comparison of the compressible triple-deck solutions with DNS results

Figure 4(a) compares the streamwise distribution of $\tilde{U}_{\tilde{Y}}|_w$, $\tilde{T}_{\tilde{Y}}|_w$, and $\tilde{P}$ rescaled by the lower-deck scaling for case M1T1R1-1, where $\tilde{P}$ for DNS denotes the pressure at the wall. The agreement of $\tilde{T}_{\tilde{Y}}|_w$ between the two curves is excellent; although the triple-deck predictions of $\tilde{U}_{\tilde{Y}}|_w$ and $\tilde{P}$ are less accurate compared to the DNS results, they have already captured the overall trend. Figure 4(b) shows a good agreement of the lower-deck temperature profiles obtained by the

TABLE II. Parameters of the case studies for different oncoming conditions and HCSs.

Case	Mach number M	Oncoming temperature T_∞	Wall temperature T_w	Reynolds number R	HCS intensity Θ_m	HCS width $\frac{d^*}{\delta_{99}\delta^*}$	Dimensionless HCS width d	Triple-deck HCS width D	$\mathcal{D}_1$	$\mathcal{D}_2$
M1T1R1-1	4.5	65.15K	4.4	50 000	0.5	8	0.695	1.13	−1.42	1.85
M1T2R1-1	4.5	65.15K	3.3	50 000	0.5	8	0.733	1.37	−1.29	1.56
M1T3R1-1	4.5	65.15K	2.2	50 000	0.5	8	0.797	1.89	−0.985	1.19
M1T4R1-1	4.5	65.15K	1.1	50 000	0.5	8	0.931	3.87	−0.528	0.673
M1T5R1-1	4.5	226.5K	4.4	50 000	0.5	8	0.706	1.11	−1.29	1.64
M1T6R1-1	4.5	226.5K	3.3	50 000	0.5	8	0.749	1.34	−1.12	1.44
M1T7R1-1	4.5	226.5K	2.2	50 000	0.5	8	0.813	1.81	−0.863	1.11
M1T8R1-1	4.5	226.5K	1.1	50 000	0.5	8	0.936	3.35	−0.559	0.728
M1T8R2-1	4.5	226.5K	1.1	25 000	0.5	8	1.11	3.99	−0.659	0.869
M1T8R3-1	4.5	226.5K	1.1	10 000	0.5	8	1.40	5.02	−0.821	1.10
M1T8R1-2	4.5	226.5K	1.1	50 000	1.0	8	0.936	3.35	−1.08	1.67
M1T8R1-3	4.5	226.5K	1.1	50 000	−0.5	8	0.936	3.35	0.625	−0.490
M1T8R1-4	4.5	226.5K	1.1	50 000	0.5	4	0.468	1.68	−0.297	0.370
M1T8R1-5	4.5	226.5K	1.1	50 000	0.5	2	0.234	0.839	−0.140	0.165
M2T1R1-1	5.92	48.69K	6.95	131 820	0.5	8	0.495	0.933	−1.44	1.74
M2T2R1-1	5.92	48.69K	5.21	131 820	0.5	8	0.512	1.12	−1.17	1.41
M2T3R1-1	5.92	48.69K	3.48	131 820	0.5	8	0.542	1.51	−1.01	1.19
M2T4R1-1	5.92	48.69K	1.74	131 820	0.5	8	0.600	2.99	−0.463	0.560
M2T9R3-1	5.92	226.5K	0.5	26 364	0.5	8	1.04	15.6	−0.337	0.419

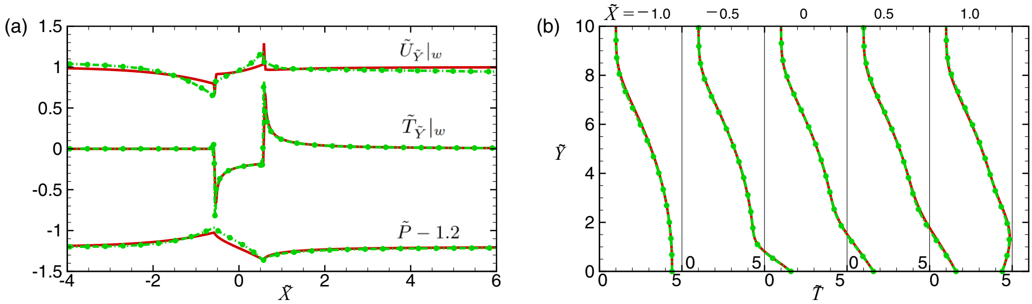

FIG. 4. Comparison of the lower-deck base flow between the triple-deck calculation (red solid lines) and DNS result (green dashed lines) for case M1T1R1-1. (a) Streamwise evolution of the wall velocity shear $\tilde{U}_{\tilde{Y}}|_w$, the wall temperature gradient $\tilde{T}_{\tilde{Y}}|_w$ and the wall pressure $\tilde{P}$, where $\tilde{P}$ is shifted for plotting convenience; (b) temperature profiles at five representative stations.

triple-deck calculation and DNS. Upstream of the heating strip, the profiles agree with the Blasius solution. After passing the leading edge of the heating strip, the wall temperature immediately increases to $T_w(1+\Theta_m)$, leading to a negative temperature gradient in the near-wall region. At a further downstream position, e.g., $\tilde{X}=0$, the fluids within the lower deck are heated up, which simultaneously leads to a gradual reduction of $|\tilde{T}_{\tilde{Y}}|_w|$. After passing the trailing edge of the heating strip, the wall temperature changes to T_w immediately, and the fluids away from the wall tend to be cooled, leading to a positive temperature gradient near the wall. Although not shown, the profile tends to recover to the Blasius profile in further downstream stations. Figure 5 further compares the main-layer mean-velocity distortion $\bar{u}-U_B$, given by Eq. (29), for cases M1T1R1-1 and M1T4R1-1. Note that the normalized width of the heating strip for the latter case is greater. The agreement between the two calculations are better for the cold-wall case [Fig. 5(b)]. The reason is that in the scaling relations Eqs. (11) and (15), T_w is assumed to be of $O(1)$, but it is practically large for an adiabatic wall. In Eq. (11), it even appears with a power of $-3/2$, which leads to a relatively greater error. Nevertheless, for case M1T1R1-1, the triple-deck calculation is still able to capture the overall "C" shape of the $\bar{u}-U_B$ profiles as the DNS result shows.

C. Scattering calculations

1. Efficiency functions

It is inferred by Eq. (70) that the transmission coefficient $\mathscr{T}=\exp[-i K_0(\mathcal{D}_1+\mathscr{H}_1\mathcal{D}_2)]$ is determined by both the mean-flow distortion ($\mathcal{D}_1$ and $\mathcal{D}_2$) and the instability property ($\mathscr{H}_1$ and K_0).

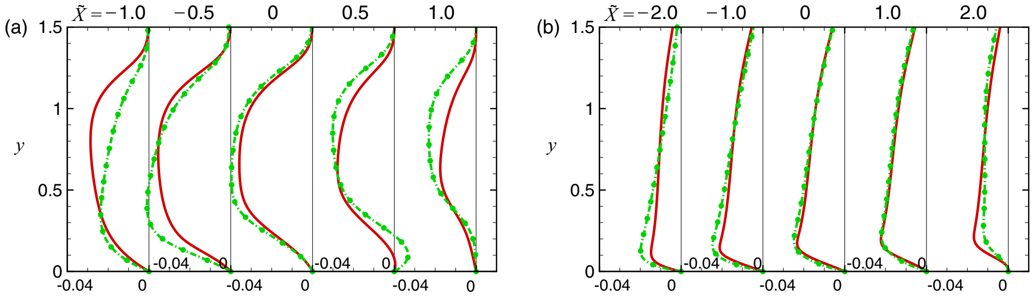

FIG. 5. Comparison of the mean-velocity distortion $\bar{u}-U_B$ between the triple-deck solution (red solid lines) and DNS (green dashed lines) for cases M1T1R1-1 (a) and M1T4R1-1 (b).

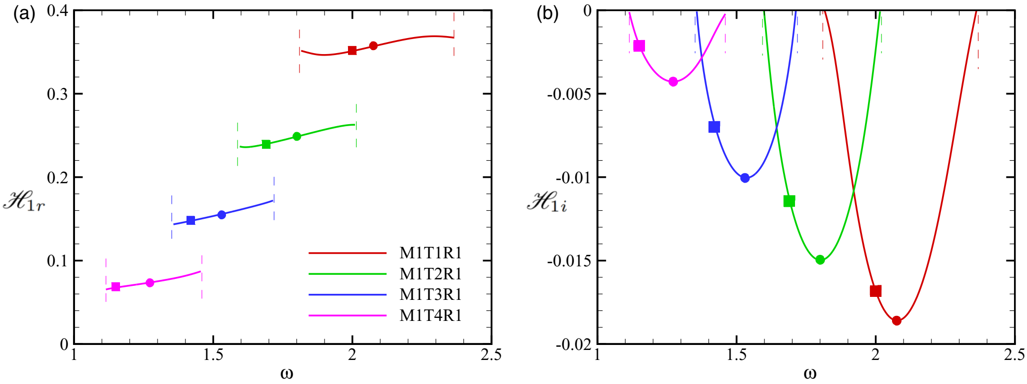

FIG. 6. Dependence on ω of the prefactor $\mathscr{H}_1$ for $(M, R, Te) = (4.5, 50\,000, 65.15K)$ (a), (b), where the vertical dashed lines represent the neutral frequencies, and the circles and rectangles denote the frequencies of the most unstable modes and the synchronization points, respectively.

The destabilizing effect appears when $\mathscr{T} > 1$, or the imaginary part of $K_0(\mathcal{D}_1 + \mathscr{H}_1\mathcal{D}_2)$ is positive, while the opposite is true for the stabilizing effect. The factors associated with the mean-flow distortion, $\mathcal{D}_1$ and $\mathcal{D}_2$, are obtained by integrating the triple-deck solutions $\tilde{A}$ and I_{T1}, respectively, and their combined effect $\mathcal{D}_1 + \mathscr{H}_1\mathcal{D}_2$ is also influenced by $\mathscr{H}_1$. Figure 6 plots the dependence of $\mathscr{H}_1$ on ω in the second-mode frequency band for cases M1T1R1 to M1T4R1. $\mathscr{H}_{1r}$ varies gently for each case, which increases with T_w monotonically. Remarkably, the imaginary part $\mathscr{H}_{1i}$ is two orders of magnitude smaller than $\mathscr{H}_{1r}$. The implication is that the value $\mathcal{D}_1 + \mathscr{H}_1\mathcal{D}_2$ (from the triple-deck calculations we know that $\mathcal{D}_1$ and $\mathcal{D}_2$ are of the same order of magnitude, but with opposite signs) stays almost real and shows rather weak dependence on ω. Therefore, the signs of $K_{0,i}$ and $\mathcal{D}_1 + \mathscr{H}_{1r}\mathcal{D}_2$ determine the stabilizing or destabilizing effect of the HCS, although the intensity of the scattering effect relies on the absolute value of the latter. For a heating strip, we know that $\mathcal{D}_1 < 0 < \mathcal{D}_2$ and $-\mathcal{D}_1 > \mathscr{H}_{1r}\mathcal{D}_2$, and so $\mathcal{D}_1 + \mathscr{H}_{1r}\mathcal{D}_2 < 0$. Therefore, a heating strip plays a destabilizing (or stabilizing) role when $K_{0,i}$ is negative (or positive). The opposite is true for a cooling strip. This explains why a heating strip and a cooling strip play the opposite roles for the same Mack frequency bands, in contrast to the roughness cases in which a hump and an indentation play the same role for the same Mack frequency bands.

Figure 7 plots the efficiency function K_0 for representative cases. As is inferred by Eq. (70), K_{0r} is related to the phase of $\mathscr{T}$, while K_{0i} determines the amplification factor. Overall, $K_{0,i}$, is positive when ω is above a critical value ω_c, but is negative for subcritical frequencies. The emergence of the critical frequency has been explained in Ref. [20]. A brief summary is as follows. The numerator of K_0 defined in Eq. (61) is almost pure imaginary for all frequencies (as proven in Ref. [20]), and the critical state appears when the real part of the denominator of K_0, i.e., $\langle \hat{\boldsymbol{\phi}}^{\dagger}, (\partial \bar{\mathbf{H}}_0/\partial\alpha)\hat{\boldsymbol{\phi}}\rangle$, crosses zero. This condition is always satisfied at a particular frequency (the critical frequency) in the second-mode frequency band in hypersonic boundary layers. The critical frequencies for cases M1T1, M1T4, M2T1, and M2T4 are $\omega_c \approx$2.1, 1.3, 2.0, and 1.3, respectively. They agree with the most unstable frequencies ω_g as illustrated in Sec. V A.

Interestingly, from simulations of the roughness-Mack interaction in adiabatic hypersonic boundary layers [17,18], it was concluded that the critical frequency ω_c is the synchronization frequency ω_s; the same conclusion was drawn for the HCS-Mack interaction [38]. This is because for adiabatic cases, the synchronization frequency ω_s is quite close to the most unstable frequency of the second mode ω_g, as illustrated in Sec. V A. However, when more cases with lower wall temperatures are considered, the difference between ω_s and ω_g becomes more appreciable, and it is clear that the critical frequency agrees with ω_g, instead of ω_s.

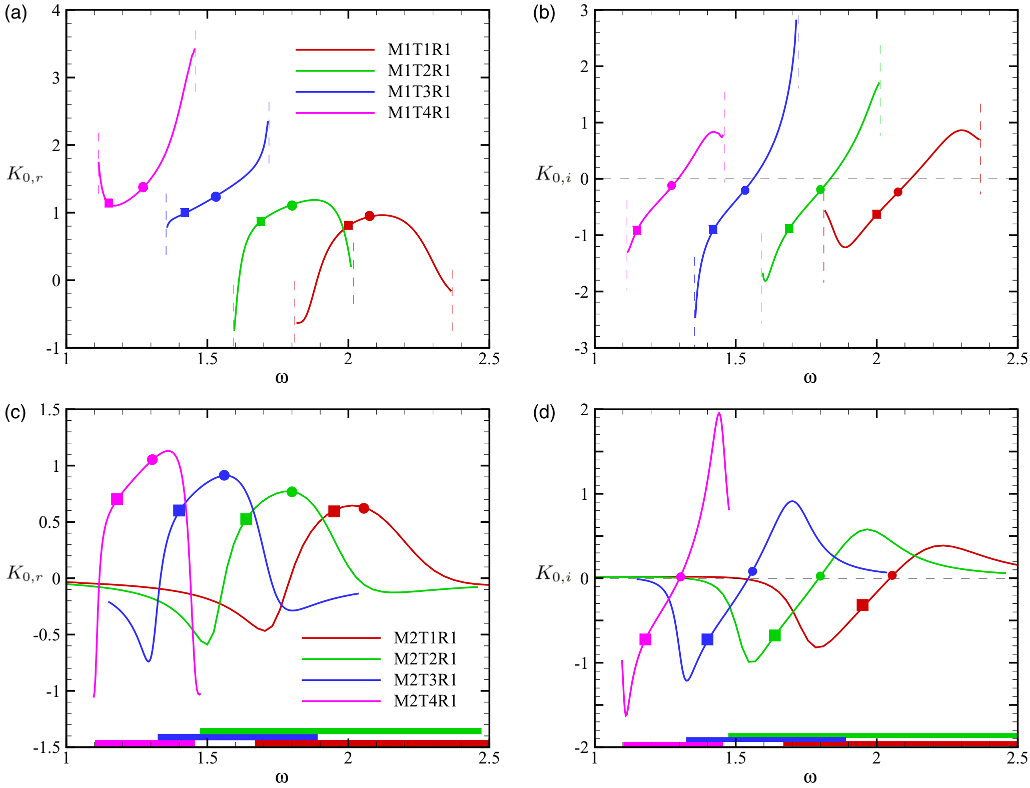

FIG. 7. Dependence of the efficiency functions $K_{0,r}$ (left column) and K_{0i} (right column) on ω for $(M, R, T_\infty) = (4.5, 50\,000, 65.15K)$ (a), (b) and $(M, R, T_\infty) = (5.92, 131\,820, 48.69K)$ (c), (d). The horizontal dashed lines in panels (b) and (d) are for $K_{0,i} = 0$. The vertical dashed lines, circles, and rectangles are the same as those in Fig. 6. The horizontal colored bars in panels (c) and (d) represent the unstable frequency bands of the second modes.

2. Comparison of the transmission coefficient between the asymptotic predictions and the numerical results

Figure 8(a) compares the perturbation temperature obtained by DNS between the cases with and without the HCS. In the upper-half plane, the colored contours show the evolution of the perturbation temperature for case H1T4R1-1 with $\omega = 1.12$, in the second-mode frequency band, while those in the lower-half plane display the perturbation evolution for the same parameters on a flat plate. The heating strip in the upper-half plane is within the region $x \in [-6.96, 6.96]$ as marked by the red line. The perturbations show two peaks: one is in the near-wall region, and the other one is at the edge of the boundary layer, which is a typical second-mode feature in a supersonic boundary layer. The mean-flow distortion of the temperature is also shown in the upper-half plane. The perturbations for both subplots show overall exponential amplifications as they propagate downstream, and the amplitude is remarkably greater when the HCS appears, indicating a destabilizing effect of the HCS on the second mode at this frequency.

Figure 8(b) plots the evolution of the temperature amplitude A_T normalized by its value at the inlet boundary for five representative frequencies. Each curve shows an exponential growing behavior, indicating a linear amplification of the sufficiently weak perturbation introduced. A kink is observed in the vicinity of the HCS center for each curve, caused by the scattering effect of the HCS. The agreement between the HLNS and DNS results is perfect. A clear illustration of the scattering of the perturbation amplitude is to normalize it by that of the flat-plate case, $\bar{A}(x) = A_T/A_{T,\text{flat}}$, as

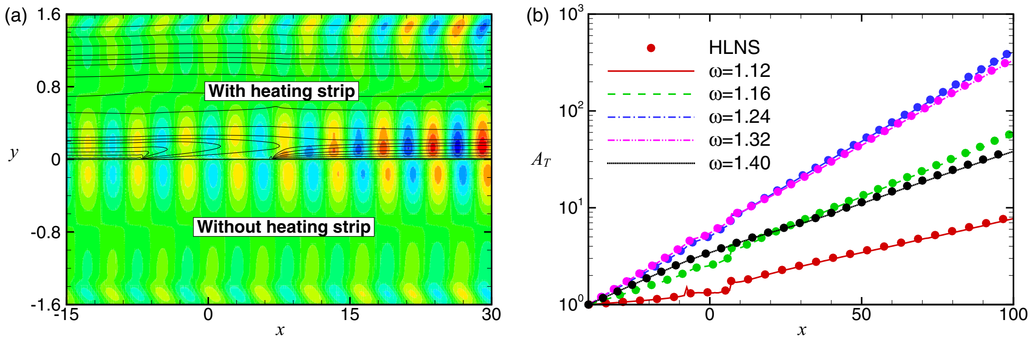

FIG. 8. (a) The perturbation temperature (colored contours) and the mean-temperature distortion (continuous lines) for case M1T4R1-1 (upper-half plane) and the flat-plate case (lower-half plane), where $\omega = 1.12$. (b) Normalized temperature amplitude obtained by the DNS (continuous curves) and HLNS (circles) approaches for case M1T4R1-1.

Fig. 9 shows for two representative frequencies (a subcritical frequency $\omega = 1.16$ and a supercritical frequency $\omega = 1.40$). The HLNS predictions agree perfectly with the DNS results. In the upstream limit, $\bar{A}$ is unity, whereas in the downstream limit, it grows like $x^{1/3}$, as the fitting curve indicates. This can be inferred by the asymptotic predictions: since $A \to X^{-2/3}$ as $X \to \infty$, as indicated by Eq. (65), the amplitude evolution given by Eq. (64) grows like $X^{1/3}$. Therefore, the transmission coefficient $\mathscr{T}$ cannot be defined as the normalized amplitude in the limit of $X \to \infty$ as for the roughness configuration (for which A decays like $X^{-5/3}$ [20]). As illustrated in Sec. III C, the transmission coefficient is defined as $\bar{A}$ at a sufficiently downstream station x_N where the asymptote has already been reached. In the asymptotic theory, the transmission coefficient, defined by Eq. (70), is also dependent on X_N, because $\mathcal{D}_1$ and $\mathcal{D}_2$ are defined by the integral of A and I_{T1} from $-\infty$ to X_N. Figure 10 shows the variation of $\mathcal{D}_1$ and $\mathcal{D}_2$ on x_N for case M1T4R1-1. Their absolute values increase with $x_N \equiv \epsilon^{-1} X_N$ like $x_N^{1/3}$, agreeing with the asymptotic predictions based on the downstream behaviours of A and I_{T1}. Using these values, we can predict the transmission coefficient for different x_N values, which are shown by the red circles in Fig. 9. For the two selected frequencies, the agreement between the HLNS calculations and the asymptotic predictions is satisfactory when x is greater than about 40 (where the asymptotic state reaches), but a trend of deviation of the two families of curves is observed as x approaches further downstream. This is because in our asymptotic theory, the nonparallel effect of the base flow, which interacts with the "wake" of the near-field perturbation and leads to a rescattering effect, is neglected, whereas in the HLNS

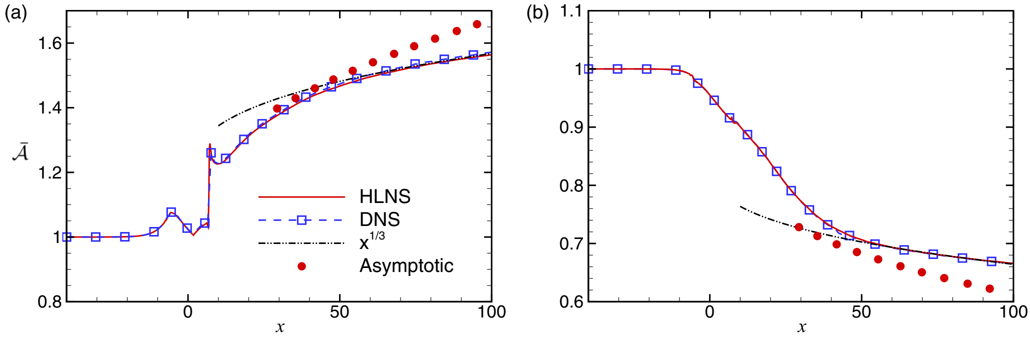

FIG. 9. Amplitude evolution normalized by that of the flat-plate case for case M1T4R1-1: (a) for ω =1.16; (b) for 1.40.

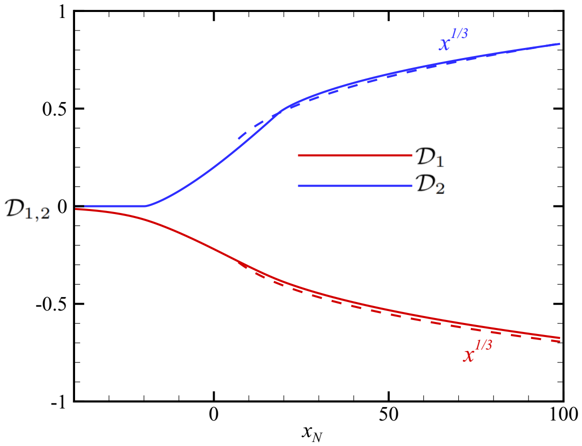

FIG. 10. Variation of $\mathcal{D}_1$ and $\mathcal{D}_2$ on $x_N \equiv \epsilon^{-1}X_N$ for case M1T4R1-1.

calculations, the nonparallelism is included. The reason why we neglect the nonparallelism in the asymptotic theory is that its effect does not appear in the leading-order terms in the inner region where $x = O(\epsilon^{-1})$. However, as x reaches the outer region where $x = O(\epsilon^{-4}\Delta^{-2})$, the nonparallel effect is accumulated to an $O(1)$ impact, modifying the transmission coefficient quantitatively; a discussion can be found in Fig. 15 of Ref. [20]. In this paper, we avoid the lengthy discussions of the effect of the nonparallelism on the transmission coefficient, because the asymptotic prediction can still be reasonably fine when x_N is not set to be too large. Therefore, for this case, we select $x_N = 50$, which is also confirmed to be a reasonable choice for other cases. Having obtained the mean flow distortions $\mathcal{D}_1$ and $\mathcal{D}_2$ in Sec. V B 2 and the efficiency functions K_0 and $\mathscr{H}_1$ in Sec. V C 1, we can predict the transmission coefficient according to Eq. (70). The solid lines in Fig. 11(a) shows the dependence of $|\mathscr{T}|$ on ω for $(M, R, T_\infty, \Theta_m, d^*/\delta_{99}) = (4.5, 50000, 65.15K, 0.5, 8)$, where four T_w values are considered. The scattering effect, measured by $||\mathscr{T}| - 1|$, of the first mode is rather weak, and so we only focus on the unstable second-mode frequency band. Reducing T_w results in a lower unstable frequency band. Each curve exhibits a critical frequency ω_c, above or below which the heating strip plays a stabilizing or destabilizing role. ω_c is rather close to the most unstable frequency of the second mode, as marked by the horizontal dot-dot-dashed lines. The HLNS calculations, shown by the dashed lines with circles, are plotted for comparison, which are confirmed to be sufficiently accurate as compared to the DNS results (crosses) for cases M1T3R1-1 and M1T4R1-1. The stabilizing or destabilizing frequency bands predicted by the asymptotic theory are confirmed by HLNS calculations. However, the asymptotic theory overpredicts appreciably the scattering effect for both supercritical and subcritical frequencies for case M1T1R1-1. As the wall temperature is reduced, the agreement becomes much better; the agreement for $T_w = 1.1$, case M1T4R1-1, is excellent. Actually, as discussed in Sec. III C, whether the HCS plays a stabilizing or destabilizing role is determined by K_0 and $\mathscr{H}_1$ (weak dependence), whereas the intensity of the scattering effect is determined by the mean-flow distortion. Therefore, the inaccuracy of the asymptotic theory for a hotter wall is attributed to the approximate nature of the triple-deck solution, as shown in Fig. 5. For each curve, the greatest error of the asymptotic prediction appears at the lower- and upper-branch neutral frequencies. This is because the Rayleigh solutions at these frequencies are less accurate due to the critical-layer effect.

Figures 11(b)–11(d) show the same comparisons as Fig. 11(a) for a different set of parameters. In Fig. 11(b), the only difference is that the temperature of the oncoming flow T_∞ is changed to 226.5K, a flight condition. The overall trend is the same, but in quantity the scattering effect is slightly weaker than the low-T_∞ cases. In Fig. 11(c), we consider the $M = 5.92$ cases, and the conclusions

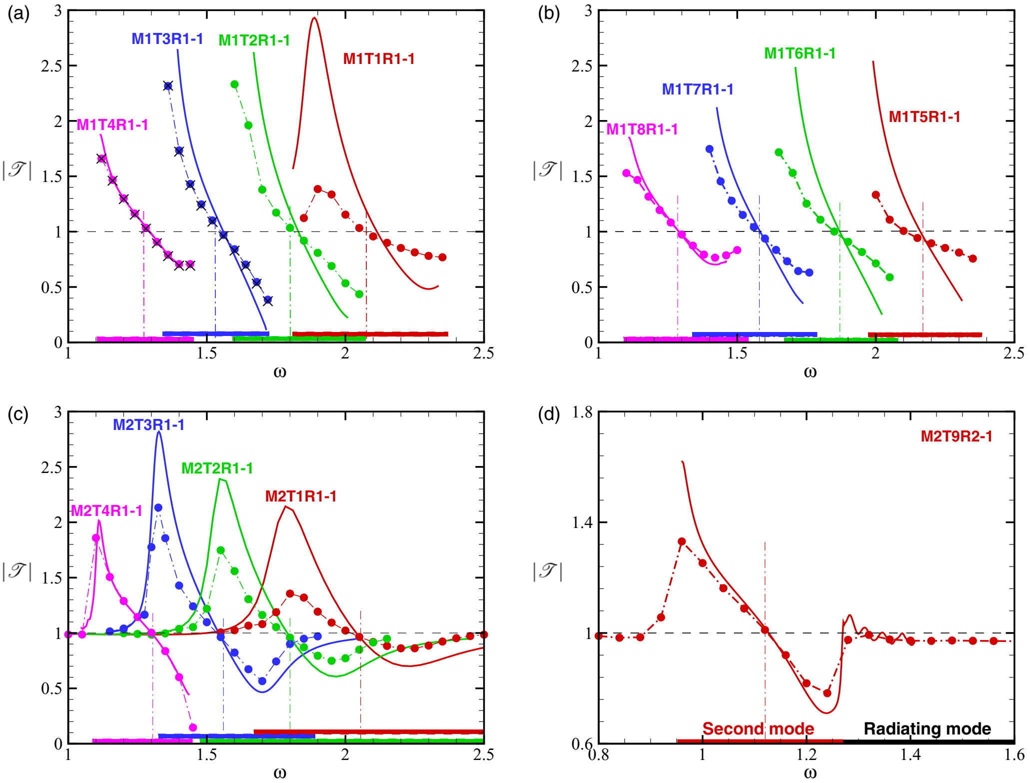

FIG. 11. Comparison of the transmission coefficient $|\mathscr{T}|$ between the asymptotic prediction and HLNS calculation for $(\Theta_m, d/\delta_{99}) = (0.5, 8)$. (a) $(M, R, T_\infty) = (4.5, 50000, 65.15K)$, (b) $(M, R, T_\infty) = (4.5, 50000, 226.5K)$, (c) $(M, R, T_\infty) = (5.92, 131820, 48.69K)$, (d) $(M, R, T_\infty) = (5.92, 26364, 226.5K)$. Solid lines: asymptotic predictions; dashed lines: HLNS calculations; crosses in (a) DNS results. The vertical dot-dot-dashed lines mark the most unstable mode, and the horizontal colored bars mark the unstable frequency band of the second mode.

remain the same. Figure 11(d) particularly shows a representative case with radiating mode, in which the wall temperature is extremely cool, $T_w = 0.5 \approx 0.07T_{ad}$. In the unstable frequency band, the asymptotic predictions agree well with the HLNS calculations, except in the region near the lower-branch neutral frequency of the second mode. When the mode is in the radiating frequency band, the transmission coefficient is almost unity, indicating a rather weak scattering effect of the heating strip. Figure 12(a) shows the impact of the HCS intensity Θ_m on the transmission coefficient. Comparing case M1T8R1-2 with case M1T8R1-1, we find that the scattering effect increases with Θ_m as expected. For each ω, $\mathcal{D}_1$ and $\mathcal{D}_2$ are almost doubled when Θ_m is increased from 0.5 (case M1T8R1-1) to 1.0 (case M1T8R1-2), so is $|\mathscr{T}| - 1$. When the heating strip (case M1T8R1-1) is replaced by the cooling strip (case M1T8R1-3), the scattering effect is reversed. Such a phenomenon is in contrast to the roughness configuration [20], in which humps and indentations play the same role on the Mack modes with the same frequency band. This is readily explained by the asymptotic prediction of $\mathscr{T}$ in Eq. (70). For roughness configurations, $\mathscr{H}_1 = 1$ and $\mathcal{D}_2$ appears as the integration of the surface shape function; remarkably, the term $\mathcal{D}_1 + \mathscr{H}_1\mathcal{D}_2$ does not change its sign for both humps and indentations due to the strong nonlinear effect. However, the nonlinearity is weak for HCSs, and it is found that $\mathcal{D}_1 + \mathscr{H}_1\mathcal{D}_2$ is negative for a heating strip and positive for a cooling strip, leading to the opposite impact of the heating and cooling strips. Again, the agreement between the asymptotic predictions and HLNS calculations are quite satisfactory.

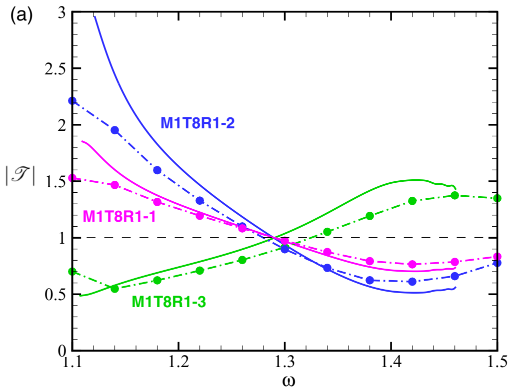

FIG. 12. Comparison of $|\mathscr{T}|$ between the asymptotic prediction and HLNS calculation for different Θ_m (a) and D (b), where $(M, T_\infty, T_w, R) = (4.5, 226.5K, 1.1, 50\,000)$. Solid lines: asymptotic predictions; dashed lines: HLNS calculations.

The impact of the HCS width D on the transmission coefficient is shown in Fig. 12(b). Decrease of D leads to a reduction of the scattering effect, which again disagrees with that for the roughness configuration. This is mainly attributed to the prefactor $\mathscr{H}_1$ in Eq. (70). For roughness configurations, as D varies, $\mathcal{D}_1$ and $\mathcal{D}_2$ vary with the same magnitude, leading to an unchanged nature of $\mathcal{D}_1 + \mathcal{D}_2$. However, for HCS configuration, since the prefactor $\mathscr{H}_1$ appears in the $\mathcal{D}_2$ term, and it is of only $O(0.1)$, the sum of $\mathcal{D}_1$ and $\mathscr{H}_1\mathcal{D}_2$ is mainly dependent on the former, leading to a positive relationship between $|\mathcal{D}_1 + \mathscr{H}_1\mathcal{D}_2|$ and D. In Fig. 13, we plot the $|\mathscr{T}|$-ω curves for three Reynolds numbers. The scattering effect increases with decrease of R monotonically, which is again different from the roughness configuration. The explanation is as follows. For fixed d^*/δ_{99}, as R decreases, the width of the roughness or the HCS under the triple-deck scaling D increases. As explained in Ref. [20], increase of D does not lead to an apparent change of the transmission coefficient, and the positive dependence of the scattering effect on R is caused by the positive dependence of $K_{0,i}$ on R. However, as explained in the last paragraph, for the HCS configuration, increase of D leads to

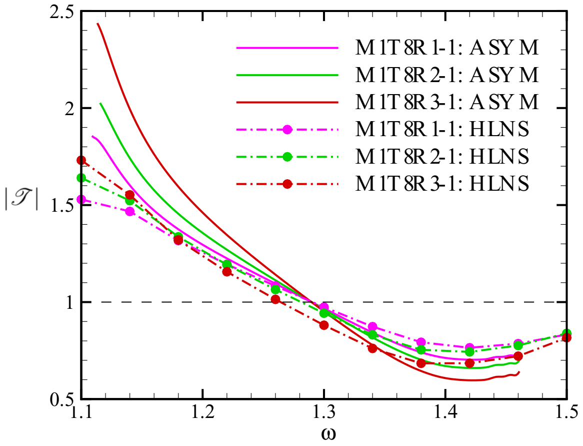

FIG. 13. Comparison of $|\mathscr{T}|$ between the asymptotic prediction and HLNS calculation for $R = 50\,000$, 25 000, and 10 000, where $(M, T_\infty, T_w, \Theta_m, d/\delta_{99}) = (4.5, 226.5, 1.1, 0.5, 8)$. Solid lines: asymptotic predictions; dashed lines: HLNS calculations.

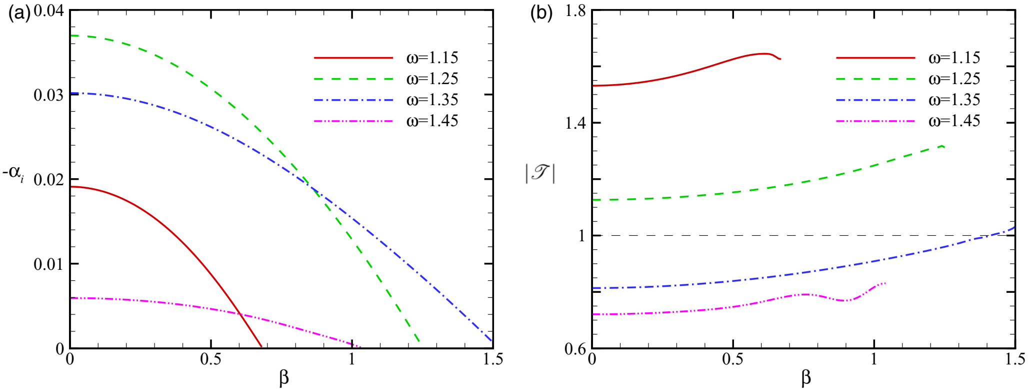

FIG. 14. Asymptotic predictions of the growth rate (a) and the transmission coefficient (b) on the spanwise wave number β for case M1T8R1-1.

a much stronger scattering effect, and such an effect overwhelms the positive dependence of $K_{0,i}$ on R, leading to the negative dependence of the scattering effect on R. Now we consider the 3D effect of the scattering process. Here, the heating strip (with $\Theta_m = 0.5$) is still taken to be 2D, but the oncoming Mack mode is 3D. Choosing case M1T8R1-1 with four representative frequencies in the unstable second-mode frequency band, Fig. 14(a) shows the dependence of the growth rate $-\alpha_i$ on the spanwise wave number β. The growth rate damps with increase of β for each frequency, and the damping rate is higher for a lower frequency. Figure 14(b) shows the transmission coefficient, $|\mathscr{T}|$, which increases with β overall, indicating that the 3D effect of the oncoming Mack mode for a heating strip leads to a stronger destabilizing effect or a weaker stabilizing effect. For $\omega = 1.35$, we see that the heating strip plays a stabilizing role when $\beta < 1.4$, whereas it enhances the oncoming Mack mode for higher spanwise wave numbers. Although not shown, the 3D effect for a cooling strip leads to a weaker destabilizing effect or a stronger stabilizing effect.

VI. CONCLUDING REMARKS AND DISCUSSION

In this paper, we develop a large-R asymptotic theory to describe the effect of 2D HCSs on both 2D and 3D oncoming inviscid Mack instabilities in supersonic or hypersonic boundary layers. This work is for a canonic problem to shed light on the physical mechanisms by which surface imperfections impact on boundary-layer transition to turbulence. In the asymptotic analysis, the width of the HCS is taken to be of $O(R^{1/4}\delta^*)$, and the mean-flow distortion can be described by the triple-deck formalism even when the intensity of the HCS Θ_m is of $O(1)$. Being different from the roughness-Mack interaction [20], the HCS-Mack interaction is more complicated because the lower deck is compressible to leading-order accuracy. Numerical calculations of the nonlinear compressible triple-deck system with the Sutherland's viscosity law are conducted, which is superior to the existing calculations [43–45] with Chapman viscosity and unity Prandtl number.

The inviscid Mack modes, including the first modes with the oblique angle smaller than $\tan^{-1}\sqrt{M^2-1}$ and all the higher-order modes, are described by the solutions of the Rayleigh equation in the main layer, combined with a viscous correction from the underneath Stokes layer. The interaction between the HCS and the oncoming Mack modes is quantified by an explicit model obtained by the multiscale analysis in the large-R asymptotic framework. The asymptotic theory reveals that the HCS plays an equivalent role as the roughness, showing two interaction regimes: (1) the HCS induces a displacement effect to the mean flow in the main deck, which distorts the oncoming perturbation directly; (2) the HCS interacts with the Mack modes in the lower deck and the Stokes layer, generating an inhomogeneous unsteady outflux to the main-layer Rayleigh equation. Following Refs. [14,20], the overall effect of the HCS on the oncoming mode is characterized by a transmission coefficient, which measures the change of the asymptotic amplitude of the instability at the localized HCS and can be readily converted to the shift of the transition location. An explicit model to calculate the transmission coefficient is presented, in which the impact of the mean-flow distortion and the instability property are readily separated.

A systematic study, based on different Mach numbers, Reynolds numbers, wall temperatures and HCS intensities, is presented. It is found that a heating (cooling) strip enhances (suppresses) the inviscid modes with frequencies lower than a critical value, whereas the stabilizing (destabilizing) effect appears for supercritical frequencies. It is confirmed from all the case studies that the critical frequency is the most unstable frequency of the second mode, instead of the synchronization frequency as in some previous works, although the two frequencies are close to each other in a few cases. Notably, three phenomena in contrast to the roughness configuration [20] are found, namely, (1) a hump and an indentation play the same stabilizing or destabilizing role on the inviscid modes with the same frequency band, but a heating strip and a cooling strip play the opposite role, (2) increase of the roughness width does not affect the scattering effect apparently, but increase of the HCS width leads to a stronger scattering effect, and (3) reducing the Reynolds number leads to a less pronounced scattering effect for a HCS configuration, but it leads to a stronger scattering effect for a roughness configuration. All of these are readily explained by our asymptotic theory. For a 3D oncoming Mack mode propagating over a heating strip, increase of its spanwise wave number leads to a weaker stabilizing role or a stronger destabilizing role, but the opposite is true for a cooling strip.

The solutions of the asymptotic theory are compared to the Harmonic linearized Navier-Stokes (HLNS) calculations and direct numerical simulation (DNS) results, and favorable agreement is achieved especially when the wall temperature of the boundary layer is low. Although the asymptotic prediction is less accurate for a higher wall temperature due to the approximate nature of the triple-deck solutions, the overall trend of the interaction process is well captured by the asymptotic theory.

ACKNOWLEDGMENTS

The work is supported by National Science Foundation of China (Grants No. U20B2003, No. 11772224, No. 12002235, and No. 91952202) and Strategic Priority Research Program, CAS (Grant No. XDB22040104).

APPENDIX A: NUMERICAL APPROACH FOR SOLVING THE COMPRESSIBLE TRIPLE-DECK SYSTEM AND ITS VERIFICATION

1. Numerical details

We re-express the nonlinear system Eq. (23) in terms of a group of first-order differential equations,

$$\tilde{U}_{\tilde{X}} + \tilde{V}_{\mathrm{DH},\tilde{Y}_{\mathrm{DH}}} = 0, \quad -\tilde{U}\tilde{V}_{\mathrm{DH},\tilde{Y}_{\mathrm{DH}}} + \tilde{V}_{\mathrm{DH}}\tilde{U}_{\tilde{Y}_{\mathrm{DH}}} + \tilde{T}\tilde{P}_{\tilde{X}} - \frac{\partial \tilde{g}}{\partial \tilde{Y}_{\mathrm{DH}}} = 0, \tag{A1a,b}$$

$$\tilde{U}\tilde{T}_{\tilde{X}} + \tilde{V}_{\mathrm{DH}}\tilde{T}_{\tilde{Y}_{\mathrm{DH}}} - \frac{1}{\mathrm{Pr}}\frac{\partial \tilde{h}}{\tilde{Y}_{\mathrm{DH}}} = 0, \quad \tilde{g} = \tilde{\mu}_{\mathrm{DH}}\frac{\partial \tilde{U}}{\partial \tilde{Y}_{\mathrm{DH}}} \quad \tilde{h} = \tilde{\mu}_{\mathrm{DH}}\frac{\partial \tilde{T}}{\partial \tilde{Y}_{\mathrm{DH}}}, \tag{A1c,d,e}$$

where $\tilde{U}$, $\tilde{V}_{\mathrm{DH}}$, $\tilde{T}$, $\tilde{P}$, $\tilde{g}$, and $\tilde{h}$ are to be solved. Note that Eq. (A1a) has been substituted into the convection term $\tilde{U}_{\tilde{X}}$ in Eq. (A1b).

The computational domain is selected as $\tilde{X} \in [\tilde{X}_0, \tilde{X}_I]$, $\tilde{Y}_{\mathrm{DH}} \in [0, \tilde{Y}_{\mathrm{DH},J}]$, and $I+1$ and $J+1$ nonuniform grid points that are clustered near $(\tilde{X}, \tilde{Y}_{\mathrm{DH}}) = (0, 0)$ are employed in the streamwise and transverse directions, respectively. Each grid point is denoted by $(\tilde{X}_i, \tilde{Y}_{\mathrm{DH},j})$, and the grid spacings Δ_i and Δ_j are defined as $\tilde{X}_i - \tilde{X}_{i-1}$ and $\tilde{Y}_{\mathrm{DH},j} - \tilde{Y}_{\mathrm{DH},j-1}$, respectively. The equations are discretized at the half point $(i - \frac{1}{2}, j - \frac{1}{2})$, such that a two-point second-order difference scheme is formed. $\tilde{U}_{i,j}$ and $\tilde{T}_{i,j}$ denote the corresponding values at $(\tilde{X}_i, \tilde{Y}_{\mathrm{DH},j})$, whereas $\tilde{V}_{\mathrm{DH},i,j}$, $\tilde{g}_{i,j}$ and $\tilde{h}_{i,j}$ denote the corresponding values at $(\tilde{X}_{i-1/2}, \tilde{Y}_{\mathrm{DH},j})$. $\tilde{P}_i$ represents the pressure at $\tilde{X}_i$, whereas $\tilde{A}_i$ the displacement function at $\tilde{X}_{i-1/2}$. Thus, the nonlinear system Eq. (A1) is discretized as

$$\frac{\Delta_j}{2\Delta_i}(\tilde{U}_{i,j}+\tilde{U}_{i,j-1})+(\tilde{V}_{\mathrm{DH},i,j}-\tilde{V}_{\mathrm{DH},i,j-1})=\frac{\Delta_j}{2\Delta_i}(\tilde{U}_{i-1,j}+\tilde{U}_{i-1,j-1}), \tag{A2a}$$

$$\left(\tilde{U}_{i-\frac{1}{2},j-1}\tilde{V}_{\mathrm{DH},i,j}-\tilde{U}_{i-\frac{1}{2},j}\tilde{V}_{\mathrm{DH},i,j-1}\right)+(\tilde{g}_{i,j}-\tilde{g}_{i,j-1})=\frac{\Delta_j}{\Delta_i}\tilde{T}_{i-\frac{1}{2},j-\frac{1}{2}}(\tilde{P}_i-\tilde{P}_{i-1}), \tag{A2b}$$

$$\begin{aligned}&\frac{\Delta_j}{2\Delta_i}\tilde{U}_{i-\frac{1}{2},j-\frac{1}{2}}(\tilde{T}_{i,j}+\tilde{T}_{i,j-1})+\frac{\Delta_j(\tilde{V}_{\mathrm{DH},i,j}+\tilde{V}_{\mathrm{DH},i,j-1})}{4\tilde{\mu}_{\mathrm{DH},i,j}}(\tilde{h}_{i,j}+\tilde{h}_{i,j-1})\\&\quad-\frac{1}{\mathrm{Pr}}(\tilde{h}_{i,j}-\tilde{h}_{i,j-1})=\frac{\Delta_j}{2\Delta_i}\tilde{U}_{i-\frac{1}{2},j-\frac{1}{2}}(\tilde{T}_{i-1,j}+\tilde{T}_{i-1,j-1}),\end{aligned} \tag{A2c}$$

$$\tilde{U}_{i,j}-\tilde{U}_{i,j-1}-\frac{\Delta_j}{\tilde{\mu}_{\mathrm{DH},i,j}}(\tilde{g}_{i,j}+\tilde{g}_{i,j-1})=-(\tilde{U}_{i-1,j}-\tilde{U}_{i-1,j-1}), \tag{A2d}$$

$$\tilde{T}_{i,j}-\tilde{T}_{i,j-1}-\frac{\Delta_j}{\tilde{\mu}_{\mathrm{DH},i,j}}(\tilde{h}_{i,j}+\tilde{h}_{i,j-1})=-(\tilde{T}_{i-1,j}-\tilde{T}_{i-1,j-1}), \tag{A2e}$$

where $\tilde{\mu}_{\mathrm{DH},i,j}=\tilde{\mu}_{\mathrm{DH}}(\tilde{T}_{i-\frac{1}{2},j-\frac{1}{2}})$, and $\tilde{U}_{i-\frac{1}{2},j-\frac{1}{2}}$ and $\tilde{T}_{i-\frac{1}{2},j-\frac{1}{2}}$ are the average of the corresponding values at the four surrounding points. $\tilde{U}_{i-\frac{1}{2},j}$ in Eq. (A2b) denotes $(\tilde{U}_{i,j}+\tilde{U}_{i-1,j})/2$.

The problem is solved by the following iterative method:

(i) Set the initial flow field as $(\tilde{U}, \tilde{V}_{\mathrm{DH}}, \tilde{T}, \tilde{g}, \tilde{h}, \tilde{A}, \tilde{P})=(\tilde{Y}_{\mathrm{DH}}, 0, 1, 1, 0, 0, 0)$.

(ii) Express the discretized system Eq. (A2) with boundary conditions in terms of an inhomogeneous linear system,

$$\tilde{\boldsymbol{\Gamma}}_i\tilde{\boldsymbol{f}}_i=\tilde{\boldsymbol{r}}^{(i-1)}, \tag{A3}$$

where $\tilde{\boldsymbol{f}}_i=(\tilde{V}_{\mathrm{DH},i,0}, \tilde{U}_{i,0}, \tilde{T}_{i,0}, \tilde{g}_{i,0}, \tilde{h}_{i,0}, \tilde{V}_{\mathrm{DH},i,1}, \tilde{U}_{i,1}, \cdots, \tilde{V}_{\mathrm{DH},i,J}, \tilde{U}_{i,J}, \tilde{T}_{i,J}, \tilde{g}_{i,J}, \tilde{h}_{i,J})^T$, and the argumented coefficient matrix $\tilde{\boldsymbol{\Gamma}}_i^+=[\tilde{\boldsymbol{\Gamma}}_i|\tilde{\boldsymbol{r}}^{(i-1)}]$ has the form

$$\tilde{\boldsymbol{\Gamma}}_i^+=\left[\begin{array}{ccccc|c}\bar{C}_0 & & & & & \bar{r}_0^{(i-1)}\\ C_1 & D_1 & & & & r_1^{(i-1)}\\ & C_2 & D_2 & & & r_2^{(i-1)}\\ & & \cdots & \cdots & & \cdots\\ & & & C_J & D_J & r_J^{(i-1)}\\ & & & & \bar{D}_{J+1} & \bar{r}_{J+1}^{(i-1)}\end{array}\right],$$

with

$$\bar{C}_0=\begin{bmatrix}1&0&0&0&0\\0&1&0&0&0\\0&0&1&0&0\end{bmatrix},\quad \bar{D}_{J+1}=\begin{bmatrix}0&0&0&1&0\\0&0&1&0&0\end{bmatrix},$$

$$C_j=\begin{bmatrix}-1 & \frac{\Delta_j}{2\Delta_i} & 0 & 0 & 0\\ 0 & -1 & 0 & -d_j & 0\\ 0 & 0 & -1 & 0 & -d_j\\ -\tilde{U}_{i-\frac{1}{2},j} & 0 & 0 & -1 & 0\\ 0 & 0 & \frac{\Delta_j}{2\Delta_i}\tilde{U}_{i-\frac{1}{2},j-\frac{1}{2}} & 0 & \frac{\tilde{V}_{\mathrm{DH}i,j}+\tilde{V}_{\mathrm{DH}i,j-1}}{4}d_j+\frac{1}{\mathrm{Pr}}\end{bmatrix},$$

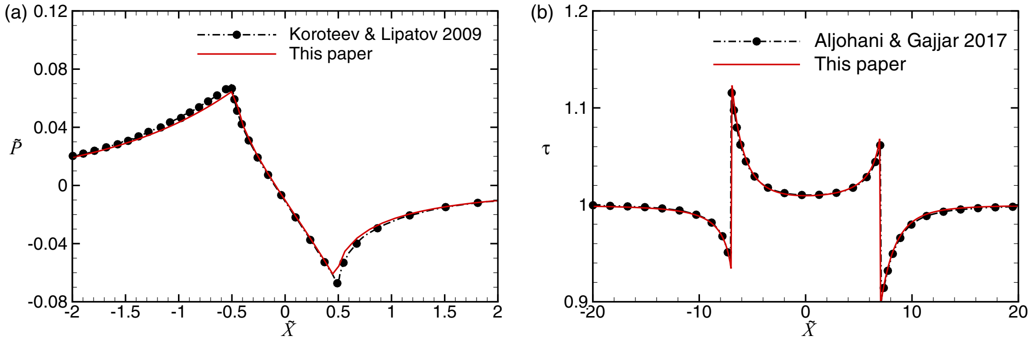

FIG. 15. Comparisons of the present results with reference results: (a) for a supersonic case [42]; (b) for a subsonic case [44].

$$D_j = \begin{bmatrix} 1 & \frac{\Delta_j}{2\Delta_i} & 0 & 0 & 0 \\ 0 & 1 & 0 & -d_j & 0 \\ 0 & 0 & 1 & 0 & -d_j \\ \tilde{U}_{i-\frac{1}{2},j-1} & 0 & 0 & 1 & 0 \\ 0 & 0 & \frac{\Delta_j}{2\Delta_i}\tilde{U}_{i-\frac{1}{2},j-\frac{1}{2}} & 0 & \frac{\tilde{V}_{\mathrm{DH}i,j}+\tilde{V}_{\mathrm{DH}i,j-1}}{4}d_j - \frac{1}{\mathrm{Pr}} \end{bmatrix},$$

$$\tilde{\boldsymbol{r}}_j^{(i-1)} = \begin{bmatrix} \frac{\Delta_j}{2\Delta_i}(\tilde{U}_{i-1,j}+\tilde{U}_{i-1,j-1}) \\ -(\tilde{U}_{i-1,j}-\tilde{U}_{i-1,j-1}) \\ -(\tilde{T}_{i-1,j}-\tilde{T}_{i-1,j-1}) \\ \Delta_j\tilde{T}_{i-\frac{1}{2},j-\frac{1}{2}}\Delta\tilde{P}_{i-1} \\ \frac{\Delta_j}{2\Delta_i}\tilde{U}_{i-\frac{1}{2},j-\frac{1}{2}}(\tilde{T}_{i-1,j}+\tilde{T}_{i-1,j-1}) \end{bmatrix}, \quad \begin{aligned} & d_j = \Delta_j/\tilde{\mu}_{\mathrm{DH},i,j}, \\ & \Delta\tilde{P}_{i-1} = (\tilde{P}_i - \tilde{P}_{i-1})/\Delta_i, \\ & \tilde{r}_0^{(i-1)} = [0, 0, 1+\Theta_m f(\tilde{X}_i)]^T, \\ & \tilde{r}_{J+1}^{(i-1)} = (1, 1)^T. \end{aligned}$$

The unshown elements in $\tilde{\boldsymbol{\Gamma}}_i^+$ are all zero.

We solve for $\tilde{\boldsymbol{f}}_i$ from the linear system Eq. (A3) by marching from $i = 1$ to I, where the elements associated with i in $\tilde{\boldsymbol{\Gamma}}_i^+$ are given by the previous iteration (or the initial values for the first iteration).

(iii) When a sweep is over, we calculate $\tilde{A}_i^{\mathrm{new}}$ and $\tilde{P}_i^{\mathrm{new}}$ by

$$\tilde{A}_i^{\mathrm{new}} = \frac{1}{2}(\tilde{U}_{i,J}+\tilde{U}_{i-1,J}) - \sum_{j=1}^{J}\frac{1}{4}(\tilde{T}_{i,j-1}+\tilde{T}_{i-1,j-1}+\tilde{T}_{i,j}+\tilde{T}_{i-1,j})\Delta_j,$$

$$\tilde{P}_i^{\mathrm{new}} = \begin{cases} -\frac{\tilde{A}_{i+1}^{\mathrm{new}}-\tilde{A}_i^{\mathrm{new}}}{0.5(\Delta_i+\Delta_{i+1})} & \text{for } i = 1 \sim I-1, \\ \tilde{P}_{I-1}^{\mathrm{new}} & \text{for } i = I. \end{cases}$$

An under-relaxation method is employed for updating $\tilde{P}$ and $\tilde{A}$. For instance, $\tilde{P}$ is updated by $\tilde{P} + \sigma(\tilde{P}^{\mathrm{new}} - \tilde{P})$, where σ is an under-relaxation factor ranging from 0.001 to 0.01.

(iv) Repeat the iteration from step (ii) until the condition $\sum_{i=1}^{I}|\tilde{A}_i^{\mathrm{new}} - \tilde{A}_i| \leqslant 10^{-6}$ is satisfied.

2. Verification of our code for triple-deck calculations

To verify our code for the triple-deck calculations, Fig. 15 compares our numerical solutions with the existing results, an analytical solution for a supersonic configuration [42] and a numerical result for a subsonic configuration [44]. Note that for subsonic flows, the P-D relation Eq. (28) is replaced by $\tilde{P}(\tilde{X}) = \pi^{-1}\int_{-\infty}^{\infty}\tilde{A}(\xi)/(\tilde{X}-\xi)d\xi$. For both calculations, the Chapman viscosity law and the unity Prandtl number are used to be coincide with the reference results. Good agreement is achieved, confirming the accuracy of our numerical solutions.

APPENDIX B: NUMERICAL APPROACH FOR SOLVING THE RAYLEIGH EQUATION

The numerical approach follows Ref. [52], and here we present a brief summary for solving the Rayleigh Eq. (33) with homogeneous boundary conditions.

For a fixed X, the computational domain $y \in [0, y_J]$ is discretized into $J+1$ nonuniform grid points, which are clustered near $y=0$. Each grid point is denoted as y_j, and the grid spacing $\Delta_j = y_j - y_{j-1}$. The equations are discretized by a two-point fourth-order difference scheme,

$$\hat{\phi}_j - \hat{\phi}_{j-1} = \frac{\Delta_j}{2}\left[\left(\frac{d\hat{\phi}}{dy}\right)_j + \left(\frac{d\hat{\phi}}{dy}\right)_{j-1}\right] - \frac{\Delta_j^2}{12}\left[\left(\frac{d^2\hat{\phi}}{dy^2}\right)_j - \left(\frac{d^2\hat{\phi}}{dy^2}\right)_{j-1}\right] + O\left(\Delta_j^5\right). \tag{B1}$$

Introduce $\mathbf{B} = (d\mathbf{H}_0/dy + \mathbf{H}_0^2)$. Then, from the Rayleigh operator, $d\hat{\phi}/dy = \mathbf{H}_0\hat{\phi}$, we know that $d^2\hat{\phi}/dy^2 = \mathbf{B}\hat{\phi}$. Thus, Eq. (B1) with the homogeneous boundary conditions can be expressed in terms of a homogeneous linear system,

$$\tilde{\boldsymbol{\Gamma}}\tilde{\boldsymbol{f}} = 0, \tag{B2}$$

where $\tilde{\boldsymbol{f}} = (\hat{v}_0, \hat{p}_0, \hat{v}_1, \hat{p}_1, \ldots, \hat{v}_J, \hat{p}_J)^T$, and the coefficient matrix $\tilde{\boldsymbol{\Gamma}}$ has the form

$$\tilde{\boldsymbol{\Gamma}} = \begin{bmatrix} \bar{C}_0 & & & & \\ C_1 & D_1 & & & \\ & C_2 & D_2 & & \\ & & \cdots & \cdots & \\ & & & C_J & D_J \\ & & & & \bar{D}_{J+1} \end{bmatrix},$$

with $\bar{C}_0 = [1 \quad 0]$, $\bar{D}_{J+1} = [0 \quad 1]$, $C_j = \mathbf{I} + \frac{\Delta_j}{2}\mathbf{H}_{0,j-1} + \frac{\Delta_j^2}{12}\mathbf{B}_{j-1}$, $D_j = -\mathbf{I} + \frac{\Delta_j}{2}\mathbf{H}_{0,j} - \frac{\Delta_j^2}{12}\mathbf{B}_j$. Note that the unshown elements in $\tilde{\boldsymbol{\Gamma}}$ are all zero. Using Gaussian elimination algorithm, we can calculate the determinant of $\tilde{\boldsymbol{\Gamma}}$.

Since Eq. (B2) is an eigenvalue problem, our purpose is to solve for a complex α for a given real ω such that $|\tilde{\boldsymbol{\Gamma}}| = 0$. This can be done by use of an iterative method as follows:

(1) Give an initial guess for α, which should be close to the eigenvalue;

(2) Calculate the determinant $|\tilde{\boldsymbol{\Gamma}}|(\alpha)$ and its derivative with respect to α, $\frac{d|\tilde{\boldsymbol{\Gamma}}|}{d\alpha}(\alpha)$;

(3) Update α by the Newton method until the eigenvalue converges.

Note that to increase the stability of the numerical scheme, we can employ a second-order iterative method as in Eq. (3.15) of Ref. [52].

---

[1] Y. S. Kachanov, Physical mechanisms of laminar-boundary-layer transition, Annu. Rev. Fluid Mech. **26**, 411 (1994).

[2] L. Mack, Review of linear compressible stability theory, in *Stability of Time Dependent and Spatially Varying Flows*, edited by M. Y. Hussaini (Springer, Berlin, 1987), pp. 164–187.

[3] G. Schrauf and H. von Geyr, Simplified hybrid laminar flow control for A320 fin aerodynamic and system design. First results, in *Proceedings of the AIAA SciTech Forum, Orlando, FL* (AIAA, Reston, VA, 2020).

[4] X. Zhong and X. Wang, Direct numerical simulation on the receptivity, instability and transition of hypersonic boundary layers, Annu. Rev. Fluid Mech. **44**, 527 (2012).

[5] M. Dong and C. Li, Effect of two-dimensional short rectangular indentations on hypersonic boundary-layer transition, AIAA J. **59**, 2368 (2021).

[6] A. I. Ruban, On Tollimien-Schlichting wave generation by sound (in Russian), Izv. Akad. Nauk SSSR Mekh. Zhidk. Gaza **5**, 44 (1984).

[7] M. E. Goldstein, Scattering of acoustic waves into Tollmien-Schlichting waves by small streamwise variations in surface geometry, J. Fluid Mech. **154**, 509 (1985).

[8] M. Choudhari, Boundary-layer receptivity to three-dimensional unsteady vortical disturbances in free stream, AIAA Paper 96-0181 (1996).

[9] P. W. Duck, A. I. Ruban, and C. N. Zhikarev, Generation of Tollmien-Schlichting waves by free-stream turbulence, J. Fluid Mech. **312**, 341 (1996).

[10] X. Wu, On local boundary-layer receptivity to vortical disturbances in the free stream, J. Fluid Mech. **449**, 373 (2001).

[11] A. I. Ruban, T. Bernots, and M. A. Kravtsova, Linear and nonlinear receptivity of the boudnary layer in transonic flows, J. Fluid Mech. **786**, 154 (2016).

[12] Y. Liu, M. Dong, and X. Wu, Generation of first Mack modes in supersonic boundary layers by slow acoustic waves interacting with streamwise isolated wall roughness, J. Fluid Mech. **888**, A10 (2020).

[13] M. Dong, Y. Liu, and X. Wu, Receptivity of inviscid modes in supersonic boundary layers due to scattering of freestream sound by wall roughness, J. Fluid Mech. **896**, A23 (2020).

[14] X. Wu and M. Dong, A local scattering theory for the effects of isolated roughness on boundary-layer instability and transition: Transmission coefficient as an eigenvalue, J. Fluid Mech. **794**, 68 (2016).

[15] A. Wörner, U. Rist, and S. Wagner, Humps/steps influence on stability characteristics of two-dimensional laminar boundary layer, AIAA J. **41**, 192 (2003).

[16] K. Fujii, Experiment of two-dimensional roughness effect on hypersonic boundary-layer transition, J. Spacecraft Rockets **43**, 731 (2006).

[17] K. Fong, X. Wang, and X. Zhong, Numerical simulation of roughness effect on the stability of a hypersonic boundary layer, Comput. Fluids **96**, 350 (2014).

[18] K. Fong, X. Wang, Y. Huang, X. Zhong, G. McKiernan, R. Figher, and S. Schneider, Second mode suppression in hypersonic boundary layer by roughness: Design and experiments, AIAA J. **53**, 3138 (2015).

[19] L. Zhao, M. Dong, and Y. Yang, Harmonic linearized Navier-Stokes equation on describing the effect of surface roughness on hypersonic boundary-layer transition, Phys. Fluids **31**, 034108 (2019).

[20] M. Dong and L. Zhao, An asymptotic theory of the roughness impact on inviscid Mack modes in supersonic/hypersonic boundary layers, J. Fluid Mech. **913**, A22 (2021).

[21] R. D. Joslin, Aircraft laminar flow control, Annu. Rev. Fluid Mech. **30**, 1 (1998).

[22] G. A. Reynolds and W. S. Saric, Experiments on the stability of the flat-plate boundary layer with suction, AIAA J. **24**, 202 (1986).

[23] H. L. Reed and A. H. Nayfeh, Numerical-perturbation technique for stability of flat-plate boundary layers with suction, AIAA J. **24**, 208 (1986).

[24] Z. Huang and X. Wu, A local scattering approach for the effects of abrupt changes on boundary-layer instability and transition: A finite-Reynolds-number formulation for isolated distortions, J. Fluid Mech. **822**, 444 (2017).

[25] J. A. Masad and A. H. Nayfeh, Laminar flow control of subsonic boundary layers by suction and heat-transfer strips, Phys Fluids A **4**, 1259 (1992).

[26] R. Messing and M. J. Kloker, Investigation of suction for laminar flow control of three-dimensional boundary layers, J. Fluid Mech. **658**, 117 (2010).

[27] S. L. Chernyshev, A. P. Kiselev, and A. P. Kuryachii, Laminar flow control research at TsAGI: Past and present, Prog. Aerosp. Sci. **47**, 169 (2011).

[28] T. Friederich and M. J. Kloker, Control of the secondary cross-flow instability using localized suction, J. Fluid Mech. **706**, 470 (2012).

[29] K. S. G. Krishnan, O. Bertram, and O. Seibel, Review of hybrid laminar flow control, Prog. Aerosp. Sci. **93**, 24 (2017).

[30] J. Zahn and U. Rist, Active and natural suction at forward-facing steps for delaying laminar-turbulent transition, AIAA J. **55**, 1343 (2017).

[31] L. Zhao and M. Dong, Effect of suction on laminar-flow control in subsonic boundary layers with forward-/backward-facing steps, Phys. Fluids **32**, 054108 (2020).

[32] D. W. Dunn and C. C. Lin, On the role of three-dimensional disturbances in the stability of supersonic boundary layers, J. Aero. Sci. **20**, 577 (1953).

[33] A. V. Dovgal, V. Y. Levchenko, and V. A. Timofeev, *Laminar-Turbulent Transition*, edited by D. Arnal and R. Michel (Springer-Verlag, Berlin, 1990), pp. 113–121.

[34] L. M. Mack, Boundary-layer stability theory, AGARD Report No. 709, Part 3 (1984).

[35] A. Sidorenko, Y. Gromyko, D. Bountin, P. Polivanov, and A. Maslov, Effect of the local wall cooling/heating on the hypersonic boundary layer stability and transition, Prog. Flight Phys. **7**, 549 (2015).

[36] V. G. Soudakov, A. V. Fedorov, and I. V. Egorov, Stability of high-speed boundary layer on a sharp cone with localized wall heating or cooling, Prog. Flight Phys. **7**, 569 (2015).

[37] A. Fedorov, V. Soudakov, I. Egorov, A. Sidorenko, Y. Gromyko, D. Bountin, P. Polivanov, and A. Maslov, High-speed boundary-layer stability on a cone with localized wall heating or cooling, AIAA J. **53**, 2512 (2015).

[38] R. Zhao, C. Y. Wen, X. D. Tian, T. H. Long, and W. Yuan, Numerical simulation of local wall heating and cooling effect on the stability of a hypersonic boundary layer, Int. J. Heat Mass Trans. **121**, 986 (2018).

[39] X. Wu and M. Dong, Entrainment of short-wavelength free-stream vortical disturbances in compressible and incompressible boundary layers, J. Fluid Mech. **797**, 683 (2016).

[40] F. T. Smith, Laminar flow over a small hump on a flat plate, J. Fluid Mech. **57**, 803 (1973).

[41] I. I. Lipatov, Disturbed boundary layer flow with local time-dependent surface heating, Fluid Dyn. **41**, 725 (2006).

[42] M. V. Koroteev and I. I. Lipatov, Supersonic boundary layer in regions with small temperature perturbations on the wall, SIAM J. Appl. Math. **70**, 1139 (2009).

[43] M. V. Koroteev and I. I. Lipatov, Local temperature perturbations of the boundary layer in the regime of free viscous-inviscid interaction, J. Fluid Mech. **707**, 595 (2012).

[44] A. F. Aljohani and J. S. B. Gajjar, Subsonic flow past localised heating elements in boundary layers, J. Fluid Mech. **821**, R2 (2017).

[45] A. F. Aljohani and J. S. B. Gajjar, Transonic flow over localised heating elements in boundary layers, J. Fluid Mech. **844**, 746 (2018).

[46] G. S. Brennan, J. S. B. Gajjar, and R. E. Hewitt, Tollmien-Schlichting wave cancellation via localised heating elements in boundary layers, J. FLuid Mech. **999**, A16 (2021).

[47] K. Stewartson, On the flow near the trailing edge of a flat plate, Mathematika **16**, 106 (1969).

[48] A. F. Messiter, Boundary layer flow near the trailing edge on a flat plate, SIAM J. Appl. Math. **18**, 241 (1970).

[49] F. T. Smith, P. Brighton, P. Jackson, and J. Hunt, On boundary-layer flow past two-dimensional obstacles, J. Fluid Mech. **113**, 123 (1981).

[50] F. T. Smith, On the first-mode instability in subsonic, supersonic or hypersonic boundary layers, J. Fluid Mech. **198**, 127 (1989).

[51] L. Lees and C. C. Lin, Investigation of the stability of the laminar boundary layer in a compressible fluid, Tech. Rep. (NASA Tech. Note-1115, 1946).

[52] M. R. Malik, Numerical methods for hypersonic boundary layer stability, J. Comput. Phys. **86**, 376 (1990).

[53] P. V. Chuvakhov and A. V. Fedorov, Spontaneous radiation of sound by instability of a highly cooled hypersonic boundary layer, J. Fluid Mech. **805**, 188 (2016).

[54] Y. Han, J. Liu, D. Xu, and J. Luo, Instability of supersonic radiation mode in hypersonic boundary layers, AIAA J. **59**, 4544 (2021).

[55] A. V. Fedorov and A. P. Khokhlov, Receptivity of hypersonic boundary layer to wall disturbances, Theor. Comput. Fluid Dyn. **15**, 231 (2002).

[56] A. Fedorov and A. Tumin, The Mack's amplitude method revisited, Theor. Comput. Fluid Dyn. **36**, 9 (2022).

[57] H. Qin and M. Dong, Boundary-layer disturbances subjected to free-stream turbulence and simulation on bypass transition, Appl. Math. Mech. Engl. Ed. **37**, 967 (2016).